RSC Advances

ROYAL SOCIETY OF CHEMISTRY

www.rsc.org/advances

Graphical abstract

Shish-kebab and β-cylindrite morphology were observed simultaneously in GAIM iPP part, which shown greatly improved mechanical properties

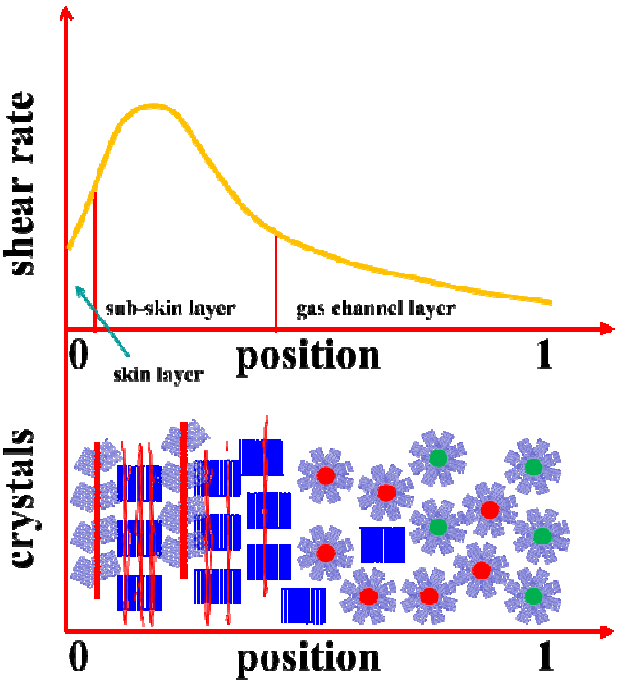

Unusual hierarchical distribution of β-crystals and improved mechanical properties of injection-molded bars of isotactic polypropylene

Long Wang, Ming-Bo Yang*

College of Polymer Science & Engineering, and the State Key Laboratory of Polymer Materials Engineering, Sichuan University, Chengdu 610065, P.R. China

Abstract:

In this study, the microstructure structures, hierarchical distribution of β-phase crystalline morphology and mechanical properties of neat isotactic polypropylene (iPP) molded by conventional injection molding (CIM) and gas-assisted injection molding (GAIM) were intensively examined. The obtained samples were characterized via two-dimensional small-angle X-ray scattering (2D SAXS), polarizing light microscopy (PLM), scanning electron microscopy (SEM), differential scanning calorimetry (DSC), wide-angle X-ray diffraction (XRD) and tensile testing. It was found that the strong shear effect introduced during the gas penetration of GAIM process greatly influences the morphologies and formation of β-crystals of pure PP specimens. Shish-kebab and β-cylindrite morphology were observed simultaneously at the sub-skin layer of GAIM part for the first time, where the flow pattern was complex and the shear strength was believed to be the greatest. Furthermore, an iPP specimen with β-crystals existed in the whole cross section of the molded bars was obtained for GAIM sample without adding β-nucleating agents or other second component. However, pure iPP sample with a low content of β-crystals were only found in the skin layer of CIM part. In addition, due the coexistence of shish-kebab and β-cylindrite structure, the mechanical properties of GAIM specimen were greatly improved when comparing with the CIM sample. Based on experimental observations, a schematic illustration was proposed to interpret the formation

* Corresponding author. Tel.: +86 28 8540 1988; Fax: +86 28 8546 0130.
E-main address: yangmb@scu.edu.cn (M.B. Yang).

mechanism of the unusual hierarchical distribution of β-crystals during GAIM process.

Key words: isotactic polypropylene; β-cylindrite; shish-kebab; mechanical property; secondary shear

Introduction

Semi-crystalline polymers are understood to crystallize in two main stages, that is, the formation of nuclei and subsequent growth of crystals. It is well known that polymer melt, under the shear field, exhibits an increased rate of crystallization or a different morphology compared with those of a quiescent melt [1]. Flow-induced crystallization (FIC) of semi-crystalline polymers, which is very common in the real industrial processing, has attracted more and more attentions [2-5]. On one hand, FIC attracts much attention for its intrinsic theoretical interest, as it is a typical example of a non-equilibrium and externally controlled phase transition process. On the other hand, FIC is also practically significant because the processing of semi-crystalline polymers constitutes the largest amount of commercially useful polymeric materials. During the most industrial processing operations (e.g., extrusion, molding, film blowing, fiber spinning, etc), the molten polymer is exposed to complex and intense flow fields and the kinetics, semi-crystalline morphology and material properties are considerably affected by the external flow field [6–8].

Gas-assisted injection molding (GAIM), an innovative technology for producing plastic parts, has received wide attention in modern industry in the past decades, owing to its flexibility in design and manufacturing of plastic part [9]. As presented in Fig. 1a, pre-determined amount of polymer melt is injected to partially fill the mold cavity. Then high pressure gas is subsequently introduced through the runner or nozzle after a short gas delay time (Fig. 1b). Finally, the gas pressure remains until all polymer material solidifies after completion of the melt filling stage (Fig. 1c). It should be noted that, during CIM process, polymer melt is merely confined by the

mold wall, i.e. a rigid and cold medium. However, during the gas penetration of GAIM process, polymer melt is confined not only by the mold wall but also by the compressed gas, and is subject to severe instantaneous flow fields during the gas penetration stage, which is much more complicated than the CIM process. As a result, many fascinating supermolecular structures (e.g. transcrystallinity, oriented crystals, spherulites with ring bands, shish kebab, etc.) were formed in the GAIM parts of high-density polyethylene, polycarbonate/polyethylene blends, glass fiber reinforced polyamide-6, and so forth [10-15].

Isotactic polypropylene (iPP) is one of the most commonly used polymeric materials, due to its versatility, relatively good mechanical properties, easy processability and recyclability and, generally, favorable price-to-performance ratio [16]. The supermolecular structure and final properties of iPP products are essentially influenced by the crystallization condition, in particular due to iPP polymorphism. There are three basic crystalline forms of iPP (α, β, γ) [17]. It has been reported that, among all the crystalline forms of iPP, the β-crystals demonstrates different performance characteristics, such as improved elongation at break and impact strength. The β-crystals can be obtained by using special techniques, such as the temperature gradient method [18], adding specific nucleating agent [19-21] or flow-induced crystallization [22-24].

In injection molding process, polymers crystallize from a melt that has been exposed to complex flow and temperature variations and a CIM part is characterized by an intrinsic heterogeneous microstructure, featuring a gradual and hierarchical variation of morphology that evolves throughout the part. Many researches concerning the microstructure of injection-molded PP bars have been carried out in recent years and great attention has been paid to the formation of different crystal forms, such as α- phase and β-phase, and their relative content in different zones along the cross section. [25-27]. However, for pure PP, the controversy on the relative content of β-phase in different zones has been an ongoing debate for a long time [28-32]. Furthermore, only a few studies have been conducted on the microstructure of pure iPP molded by GAIM and no work focusing on the formation of different

crystal forms of GAIM parts.

In this research, the hierarchical distribution of β-phase crystalline morphology and mechanical properties of neat iPP specimen molded by GAIM were investigated. For comparison, the crystalline morphology and crystal forms of its CIM counterpart were also examined. In an attempt to observe the microstructure and crystalline forms of iPP, the samples molded by different processing methods were characterized by using synchrotron two-dimensional small-angle X-ray scattering (2D SAXS), polarizing light microscopy (PLM) and scanning electron microscope (SEM). The crystalline forms and their distributions were characterized via differential scanning calorimetry (DSC) and wide-angle x-ray diffraction (WAXD). Moreover, mechanical properties of the molded bars were characterized by tensile test. From a practical point of view, attempting to explore the microstructures and crystalline morphologies of iPP during the GAIM process which has been widely used in practical production is of great significance.

Experimental

Materials

The iPP was commercially available from ExxonMobil Chemical Company Houston, Texas, USA with a melt flow index 0.9 g/10min (230 ℃, 2.16 kg). The weight average molecular weight (M_w) was 690 kg/mol.

Sample preparation

A PS40E5ASI injection molding machine and a gas pressure system (Model: MPC-01) supplied by ZhongTuo (Beijing) Co, P.R. China were utilized for the molding process. To provide an even route for gas penetration, a mold with a circular cross-section cavity was employed. It should be mentioned that a sub-cavity connected to the main cavity by a narrow flow channel was designed as shown in Fig. 1, which was different from our previous mold [33]. With this new design, it can guarantee an even and thorough penetration of the high pressure gas. The processing

parameters for GAIM process were listed in Table 1. For comparison, the conventional injection molding (CIM) was also carried out by using the same processing parameters but without gas penetration and gas-assisted packing process. It should be noted that the melt injection volume for CIM is as large as 100 vol.% and the main body of CIM part exhibits a solid structure, while the GAIM part takes on a hollowed one.

Synchrotron two-dimensional small-angle X-ray scattering (2D SAXS)

The synchrotron 2D SAXS experiments were conducted on the BL16B1 beamline in the Shanghai Synchrotron Radiation Facility (SSRF), Shanghai, China. The wavelength used was 0.124 nm, and the rectangle-shape beam had dimensions of 0.2 ×2 mm^2. The backgrounds of all the 2D SAXS patterns had been extracted. Each 2D SAXS pattern obtained in the different zones along the thickness direction of the molded bars was collected within 40 s at a sample-to-detector distance of 1950 mm. At this distance the effective scattering vector q ($q=4\pi\sin\theta/\lambda$, where 2θ is the scattering angle and λ the wavelength) range is 0.17-2.08 nm^{-1}. The samples were placed with the orientation (flow direction) perpendicular to the projection beams as shown in Fig. 2. Fit2D software from the European Synchrotron Radiation Facility was used to analyze the SAXS data and the 2D SAXS patterns were integrated azimuthally to obtain one-dimensional (1D) scattering profile as a function of azimuthal angle. For 1D SAXS data, the long period, $L = 2\pi/q$, was obtained [34-35].

Polarizing light microscopy

Molder bars were sectioned using a KD-3558 rotary microtome provided by Zhejiang Jinhua Kedi Strumntal Equipment Co., Ltd, China. Thin sections, about 10 microns in thickness, were cut from the midpoint of the bars parallel to the flow direction. These microtomed specimens were sandwiched between a glassslide and coverslip and then were observed by using a Leica DMIP polarizing light microscopy (PLM) with a Canon PowerShot 550 digital camera (DC).

Scanning electron microscopy

The selective permanganic etching approach proposed by Olley and Bassett [36] was employed to prepare the specimens for morphological observations under scanning electron microscope (SEM, Model: JSM-5900LV, JOEL Co., Ltd., Japan). Before the etching procedure, the specimen was cut in the middle of the bar along the melt flow direction; then these segments were immersed in the liquid nitrogen for about 30 min before they were cryogenically fractured. After etching, the surfaces of specimens were covered with a thin layer of gold, the crystalline morphology in different zones of these samples was observed with an accelerating voltage of 20 kV.

Differential scanning calorimetry

Thermal analysis of the samples, which were cut at various distances from the surface, was conducted in a differential scanning calorimetry (DSC, TA-Q20). All the measurements were conducted under nitrogen atmosphere. Sample about 5 mg was used and the heating rate was 10 °C/min from 25 to 160 °C. The percentage of β-crystals of iPP, ϕ_β, was determined by the relative crystallinity of α-crystals and β-crystals according to Eq. (1) given as

$$\phi_\beta = \frac{X_\beta}{X_\alpha + X_\beta} \times 100\% \quad (1)$$

where X_α and X_β are the crystallinity of the α- crystals and β- crystals, respectively, based on the measured heat of fusion.

Because of the coexistence of α-crystals and β-crystals in the molded bars, the crystallinity of each crystal forms could be calculated separately according to the following equation,

$$X_i = \frac{\Delta H_i}{\Delta H_i^0} \times 100\% \quad (2)$$

where ΔH_i is the calibrated specific fusion heat of either the α-crystals or β-crystals and ΔH_i^0 is the standard fusion heat of either pure α-crystals or β-crystals of iPP. The values of ΔH_α^0 for α-crystals and ΔH_β^0 for β-crystals were 177.0 and 168.5 J/g,

respectively [37].

DSC curves of the samples exhibited both an α-fusion peak and a β-fusion peak. The specific fusion heats for α-crystals and β-crystals were approximate according to the following calibration method. The total fusion heat, ΔH, can be obtained by integrating from 100 to 180 °C on the DSC thermogram. A vertical line was drawn through the minimum between the α- and β-fusion peaks and the total fusion heat was divided into the β-component, ΔH_β^*, and α-component, ΔH_α^*. The less perfect α-crystals melted before the maximum point during heating, so it contributed to ΔH_β^*, and consequently, the true value of β-fusion heat, ΔH_β, could be approximated by a production of multiplying ΔH_β^* with a calibration factor A [38],

$$A = [1 - (\frac{h_2}{h_1})]^{0.6} \quad (3)$$

$$\Delta H_\alpha = \Delta H - \Delta H_\beta \quad (4)$$

$$\Delta H_\beta = A \times \Delta H_\beta^* \quad (5)$$

In Eq. (3), h_1 and h_2 are the heights from the base line to the β-fusion peak and minimum point, respectively.

Wide-angle X-ray diffraction

To investigate the hierarchically crystalline structures and distribution of β-crystals of the molded bars, wide-angle X-ray diffraction (WAXD) measurements were carried out in a DX-1000 X-Ray diffractometer (Dandong Fanyuan Company, China) with curved graphite crystal filtered Cu K radiation source (λ = 0.154 nm) at 50 kV and 30 mA at 25 °C. The sample for WAXD characterization was cut from the middle section of the injection molded samples.

The relative content of β-crystals (K_β) was determined from the WAXD profiles according to the following relation,

$$K_\beta = H_\beta(300)/[H_\alpha(110) + H_\alpha(040) + H_\alpha(130) + H_\beta(300)] \quad (6)$$

where $H_\alpha(110)$, $H_\alpha(040)$, $H_\alpha(130)$ are the intensity of the (110), (040) and (130)

reflections of α-crystals in PP, appearing at 2θ around 14°, 16.8° and 18.4°, respectively; $H_\beta(300)$ is the intensity of (300) reflection of β-crystals at 2θ around 16.0° [39].

Tensile testing

As for the hollow structures of GAIM sample, the standard ASTM sample for tensile test cannot be applied directly. Then specimens with a modified shape, as shown in Fig. 3, were prepared for the tensile test. The tensile tests were conducted on an Instron universal testing machine (Model 5567) with a crosshead speed of 50 mm/min under room temperature (~25 °C). The specimen broke around the center of the specimen during the test, and the average values were obtained from over five specimens for each measuring condition.

Results and Discussion

Shear-induced orientation

Fig. 4 was the selected 2D SAXS patterns at different zones of two samples. The flow direction was vertical, and it can be considered the same as the fiber axis when assuming the deformed scatterers have a fiber symmetry [40]. It is widely accepted that the appearance of an equatorial streak in 2D SAXS patterns can be attributed to the shish-like crystalline structure, oriented parallel to the flow direction, while the appearance of meridional maxima can be attributed to kebab-like lamellar stacks, oriented perpendicularly to the flow direction [41]. As shown in Fig. 4a, 2D SAXS pattern of the skin layer of GAIM sample clearly exhibited the appearance of meridional maxima from the oriented scatterers, indicating that the packages or stacks of crystal lamellae (kebab) have already formed in the skin layer. In addition, a relatively weak equatorial streak was existed in the skin layer, which verified the existence of a shish structure parallel to the flow direction. This weak signal was mainly due to the small size or low volume fraction of shish, which was consistent with our previous results that the shear field in the skin layer was low [10-12]. As

depicted in Fig. 4b, an equatorial streak in the 2D SAXS pattern was clearly observed at the sub-skin layer of GAIM sample besides the meridional maxima, indicating that a typical shish-kebab morphology was formed in the sub-skin layer of GAIM specimen [2]. However, the preferentially aligned lamellar structure existed only in the skin and sub-skin zones of GAIM sample. As illustrated in Fig. 4c, the gas-channel zone of GAIM sample was characterized by an isotropic scattering circle, indicating the absence of any preferred orientation or very low degree of orientation within this region. Under the mutual interaction of the shear gradient introduced due to the high pressure gas penetration process and the temperature gradient across the thickness direction, hierarchical oriented structures existed from the skin to the gas-channel layer of GAIM part. For comparison, the 2D SAXS patterns of CIM sample at different zones were also investigated and illustrated in Fig. 4. It can be observed that the dominant patterns of CIM sample (Fig. 4d and 4e) from the skin to core zone were mainly characterized by isotropic rings due to chain's random orientation.

The variables of crystalline structures can be quantified in the azimuthal scans of SAXS patterns at different zones of two samples (Fig. 5). As shown in Fig. 5a, the skin layer of GAIM sample was characterized by an obvious meridional scattering as well as a weak equatorial scattering. As for the sub-skin layer of GAIM sample, Fig. 5b clearly displayed both strong meridional and obvious equatorial scattering, indicating that a typical shish-kebab morphology was formed. However, the gas channel zone only exhibited a weak and broad meridional scattering without any signal of equatorial scattering, implying formation of only less oriented arrangement of iPP lamellae. Therefore, the skin and sub-skin layers of GAIM specimen contained iPP lamellae (periodicities) oriented along and perpendicular to the fiber axis. In contrast, for the CIM sample (Fig. 5b), apart from no trace of equatorial scattering, the meridional scattering was very broad in the skin and core zones, which validated absence of shish-kebab or oriented structure in the CIM specimen.

According to the references [42-43], lamellar crystal thickness and interlamellar amorphous layer thickness can be obtained from the one-dimensional correlation

function of the SAXS patterns, but due to the difficulty and complexity of calculating the one-dimensional correlation function, we compare the contributions of the isotropic and oriented scattering instead and this may be more important for the oriented samples used in this research. To quantify better the contributions of the isotropic and oriented scattering, the total scattered intensity of the 2D SAXS patterns were separated into two contributions; isotropic and oriented, and the oriented component was calculated by subtracting the azimuthally independent component from the total SAXS intensity. Then 1-dimensional scattering profile were extracted along the meridian line as well as along the equatorial line for the anisotropic scattering patterns and averaged 1D scattering profiles was obtained for the isotropic 2D SAXS patterns [44-45]. The isotropic part of the 2D SAXS patterns was sectioned in the range of 0-180 ° and the Bragg's long spacing (L) ascribed to isotropic PP was determined. Two sections of the oriented patterns were made: (i) along the meridian (-45°–+45°) giving rise to L^{Eq} and and (ii) along the equator (45°–135°) for L^{Mer}. 1D SAXS intensity profiles of circularly integrated 2D SAXS patterns at various zones of two samples were shown in Fig. 6 and the long spacing (L), reflecting the thickness of lamellar and amorphous region between two lamellae, was obtained and listed in Table 2. For the skin layer of GAIM sample, it can be observed that the L^{Eq} (16.8 nm) was bigger than the L^{Mer} (15.9 nm). The variables of the periodicities for the sub-skin layer followed the same tendency and the corresponding periodicities of the sub-skin layer were larger than that of the skin layer, indicating larger thickness of iPP lamellae and more regularly aligned lamellae of the sub-skin layer. As for the sub-skin zone of GAIM sample, the velocity gradient between the interface of the high-pressure gas and molten polymer introduced a strong shear field during the gas penetration process. Generally, the iPP lamellae along the equator have bigger long spacings as compared to those of the iPP crystallized along the fiber direction. As shown in Table 2, one can observe that the iPP lamellae of the oriented zones (skin and sub-skin layer) of GAIM specimen have bigger periodicities than the non-oriented zones (gas channel). Furthermore, it can be seen that the GAIM iPP specimen exhibited higher long periods as compared to the pure CIM sample, indicating larger thickness of iPP

lamellae or more perfect crystal structure. This was originated from the highly melt shearing induced crystallization during the gas penetration of GAIM process. Besides, the long spacing of the core zone of CIM sample was larger than the skin layer, which was caused by the low cooling rates in the core zone of CIM sample.

Crystal morphologies of iPP

The crystal morphologies in different zones of pure iPP molded via GAIM was investigated by PLM and shown in Fig. 7. It should be emphasized that PLM provides useful information about the structure of a sample as a whole, in spite of its relatively low resolution. As depicted in Fig. 7, it shown that the molded bar fabricated by GAIM displayed a typical skin-core morphology. And when observed in the cross section, the boundary between the non-spherulitic and spherulitic zone appeared quite sharp. The corresponding areas observed parallel to the flow direction, however, were found to contain a layer between the skin and gas channel zone that was not readily apparent in the cross sections. This sub-skin layer, or what will be called the shear zone, was spherulitic, but the morphology differed from that in the gas channel zone in that the spherulites (or sheaves) in the shear zone were row nucleated while those in the gas channel zone were randomly nucleated. The appearance of the three zones in a longitudinal thin section was shown in Fig. 7a. As shown in Fig. 7b, the exterior layer (skin and shear layer) consisted of regions of small, bright spherulites exhibiting negative birefringence. The gas channel zone was formed by a spherulitic domain structure as observed in Fig. 7c. The spherulites or sheaves (oriented lamellar) in the skin and shear layer were bunched tightly together along thin, negatively birefringent rows. The spherulites that were nucleated from each row were nearly identical in size and shape; their sizes increases with increasing distance from the mold surface. The majority of the spherulites in the exterior were the negatively birefringent type III variety, characteristic of the β-crystals form of polypropylene [46]. The gas channel zone contained larger but randomly sized spherulites. With the exception of occasional type III spherulites, the spherulites in the gas channe zone were the positively birefringent type I variety which was characteristic of the stable,

monoclinic polymorph [46]. For comparison, the crystal morphologies in CIM part were also investigated, to explore the role of secondary gas penetration on the formation of different crystal forms. As shown in Fig. 7d, the trend of morphological evolution at corresponding position along the residual thickness was similar for GAIM and CIM specimens. However, the thickness of the exterior layer of GAIM sample was about 620 μm, which was much larger than that of the CIM part (about 300 μm). Elucidation of the morphological fine structure of each layer is of basic interest, as it might cast light on the mode of formation of these layers, and particularly the role that secondary gas penetration play in their formation. Since PLM cannot tell the fine structures of the molded bars, in subsequent section, scanning electron micrographs of etched samples will be presented which clearly identify some of the major fine crystalline features.

Hierarchy in crystal structuress

To obtain the fine architecture of the molded bars, morphological features of the etched iPP at different zones along the flow direction were studied by using SEM. Macroscopically, the dominating feature of GAIM sample was the shear-induced morphologies with gas channel layer in the center, highly-oriented layer surrounding the gas channel zone and the skin layer in the cross sectional areas of the specimen. Under flow field, polymer chains can be stretched and oriented into rows along the flow direction in the molten state. These prearranged rows of molecule chains can be transformed into crystalline clusters and act as crystallization nuclei of the subsequent crystallization process. And this characteristic linear type of self-nucleus is termed a row nucleus [47, 48]. Row nuclei can induce an epitaxial growth of crystallites of folded chains leading to characteristic supermolecular formations of cylindrical symmetry, cylindrites [48]. As shown in Fig. 8a, it is found that the skin layer of GAIM sample was characterized by β-cylindrites align in rows along the flow direction. Cylindritic structure is one kind of many different supermolecular formations which always corresponds to another crystalline morphology called “transcrystalline”. The difference between them is that the former developed via

homogeneous or self nucleation, while the latter formed by heterogeneous nucleation [48].

Most interestingly, compared to the skin layer, one can observe shish-kebab like fibrillar structure in the sub-skin layer (see Fig. 8b) as well as the β-cylindrites. Shish-kebab structure, which was first found in stirred polyethylene solution by Pennings and co-workers [49], is usually a predominant morphological feature when polymer crystallizes under shear flow. The so-called "shish-kebab" structure, consisting of long central fiber core (shish) and lamellar crystalline structure (kebab) periodically attached to the shish, substantially influence the final physical and mechanical properties of the component [50]. In this sub-skin zone or shear layer, as the gas penetration, the velocity gradient between gas front and melt front induced a strong shear filed, in which the shear rate might exceed the critical value for shish-kebab formation, and induced the extension and crystallization of molecular chain segments along the shear direction and developed into stable structure. The stable structure, i.e. shish, as a primary nuclei, further induced the folded-chains overgrow along the flow direction and finally the shish-kebab morphology could be formed. However, the shish kebab structures could not been observed in the skin zone probably due to the weak shear field in this region [10]. As has been mentioned, one of the most notable differences in the crystalline morphologies between the skin and sub-skin layers of GAIM sample was the existence of shish-kebab structures in the sub-skin layer. As shown in the magnified micrographs of Fig. 8c, the shish-kebab structure can be clearly seen in the sub-skin zone of GAIM sample. It is noted that it is hard to find shish-kebab structure in the skin layer of GAIM sample. However, it does not necessarily mean that there is no shish-kebab structure in the skin layer because the formed shish-kebab may be too small or too diluted to be detected. To our best knowledge, the coexistence of β-cylindrites and shish-kebab morphology is for the first time observed in pure iPP parts molded by GAIM, and the presence of β-cylindrites in injection-molded parts of neat iPP is also rarely reported. In the gas channel layer (Fig. 8d), common α-spherulites of polypropylene were obtained and the lamellae primarily showed a random arrangement with much less oriented

structures. In addition, it should be mentioned that there were some black grains in the SEM microphotographs, which may be caused by the etching procedures or the raw materials and further research should be performed. For the CIM part, the dominant morphological feature from skin to core zone was α-spherulites of polypropylene, which was similar to the gas channel zone of GAIM part (see Fig. 9).

Thermal properties

The thermal behaviors in different zones of iPP sample molded by GAIM were shown in Fig. 10, and the corresponding melting parameters were listed in Table 3. As shown in Fig. 10a, the skin and sub-skin layer of GAIM sample exhibited three endothermic melting peaks, whereas the gas channel layer of PP only exhibited a single endothermic peak at around 166 °C. The first two peaks at around 146~152 °C of the skin and shear layers of GAIM sample were caused by melting of the original β_1-crystals and subsequent recrystallization to produce a more stable structure (β_2) during scanning, while the last peak was associated with the melting of the original and recrystallized α-crystals [51]. However, such double melting phenomenon of the β-crystals was not observed in CIM sample and only a single melting peak of α-crystals was observed in Fig. 10b for both of the skin and core layer of CIM sample.

As listed in Table 3, the total fusion heat (α- and β-crystals) of GAIM sample slightly increased from the skin layer to sub-skin layer and then gas channel zone. This was firstly due to the cooling rate decreased along the residual thickness and thus the gas channel layer possessed the slowest cooling rate and then the longest time for crystallization. Moreover, the flow filed also contributed to the enhancement of crystallinity [52]. In addition, the total fusion heat at each zone of GAIM sample was larger than that of the CIM part. These differences were mainly due to the strong shear field introduced during the secondary shear process of GAIM sample. These results were firmly confirmed by the above-mentioned morphological results, which clearly shown that GAIM sample had more oriented lamellar and shish-kebab structure. There are two reasons [1], both thermodynamic and kinetic, why chain extension

enhances crystallization. On one hand, flow-induced orientation increases the melting temperature of the material, thus the crystallization temperature, i.e. the entropy of the melt is lowered hence the free energy is raised. On the other hand, the extended chain is closer to its final configuration state in a crystal, and has, therefore, less of a kinetic barrier to overcome than a chain in the random state to form a crystal structure. As a result, the GAIM part had larger values of fusion heat due to a stronger shear field and a higher cooling rate.

The percentage of β-phase, ϕ_β, was determined according to Eq. (1) and listed in Table 3. Based on the DSC results, it can be seen that only the skin and sub-skin layer of GAIM sample had β-crystals and ϕ_β of the skin and sub-skin layer was 11.48% and 17.20%, respectively. However, it does not necessarily mean that there was no β-crystals in the gas channel layer of GAIM or CIM sample, because the β→α phase transition can take place in PP during thermal treatment and this transition depends on the structure and content of the β-crystals in the molded bars that was induced by the flow field [16]. Due to the β→α phase transition can take place in PP during thermal treatment, wide-angle X-ray diffraction (WAXD) measurements were carried out in the following analysis.

Distribution of crystalline morphologies

Fig. 11 depicted the WAXD patterns of the molded bars of iPP. The reflections at 2θ angles of 14.0°, 16.8° and 18.6° correspond to the (110), (040) and (130) lattice planes of monoclinic α-crystals of iPP and the reflection at 2θ of 16° corresponds to the (300) plane of the hexagonal β-crystals of iPP [39].

As depicted in Fig. 11a, it was surprising that the β-crystals were detected in the whole cross section of GAIM sample, which was different from the above-mentioned DSC results. That is to say, by using the GAIM method, we can obtain a pure iPP sample with β-crystals existed in the whole molded bars without by adding β-nucleating agents or other second component. In previous researches, pure iPP samples with β-crystals were only found in the skin layer or core layer of molded bars depending on the different processing methods and molecular peculiars of

polypropylene [28-31], and β-nucleating agents or other second component needed to be added to obtain a part with β-crystals in the whole cross section [19-21]. To our best knowledge, this peculiar is for the first time observed in pristine iPP part molded by GAIM, which were mainly correlated with the strong shear field introduced by the secondary shear and high cooling rate of GAIM process. It has been widely accepted that the β-crystals can be formed in a sheared iPP melt [53-55], in which melt-shearing yields α-row-nuclei, the surface of these α-row-nuclei may induce an α→β transition in the crystalline modification of iPP, so that β modification was formed. Most of these studies mainly were performed under the isothermal crystallization condition at a low shear, low strain and single flow field conditions [52, 55]. However, polymer materials have been experienced more complex flow field which consists of shear, elongational, or mixed, thermal field and the interaction between melts in practical processing. As a result, our results may provide some tips for practical production of pure iPP specimen. As for CIM sample, the β-crystals of iPP only existed in the skin layer, which was in accord with other researchers studies on injection molding parts [30].

The relative content of β-phase (K_β) of molded bars were calculated according to Eq. (6) and the results were summarized in Table 3. For GAIM sample, the K_β value in the sub-skin layer was the largest and the gas-channel zone possessed the lowest K_β, which was consistent with the above hierarchical structures observed by SEM. However, there was a low value of K_β in the skin layer of CIM sample, which indicated a much lower shear field in the CIM process. Compared with CIM, the K_β value of GAIM sample was substantially increased, which indicated that the stronger shear field induced during the gas penetration of GAIM process promoted the formation of β-crystals of iPP. As shown in Table 3, it can be observed that there exist differences of β-crystals of iPP measured by DSC and WAXD methods. The obvious differences between two values of K_β and ϕ_β in Table 3 may be resulted from the occurrence of β→α phase transition during the heating process of DSC and thus the β-crystals of iPP measured by DSC was smaller than the real values. Since the WAXD measurement was performed under ambient temperature and did not destroy the

microstructure of the molded bars, it was reasonable to deem that the results of WAXD were more close to the real values.

Mechanical properties

The selective stress-strain curve of GAIM sample was shown in Fig. 12, including CIM one for comparison. There was obvious necking for both of the GAIM and CIM samples with ductile failure. The obtained values of yield stress and strain were listed in Table 4. The yield stress, a measure of the strength at the point of deviation from Hooke's law (the yield point), is important to polymeric materials. As shown in Table 4, a mechanical enhancement from 32.2 MPa of CIM sample to 43.0 MPa of GAIM sample for yield stress was observed, indicating a better strength for GAIM sample. The difference of the values of yield stress were mainly caused by the microstructure and crystalline structures among the iPP articles and the yield stress was directly proportional to the content of different crystal forms and area of the oriented zones [56, 57]. It is known that the strength of α-crystals is higher than the β-crystals of iPP. Since the content of α-crystals of GAIM was lower than the CIM sample, the higher strength of GAIM sample can be attributed to the highly area of oriented zone, which was consistent with the morphological results. Yield strain can be considered the ratio of material deformability at a low strain. It is known that its values are increasing with the ductility of material. Regarding higher ductility of β-crystals as compared to α-crystals, higher value of yield strain of GAIM sample were obtained. As is known, the strain at break represents cold drawability, the area under the stress-strain curve, in fact, manifests the work spent on the failure, i.e., specimen toughness. More importantly, there was a sharp enhancement of the strain at break of GAIM sample, which was five times larger than that of the CIM sample. As a result, the GAIM specimen was characterized by a great enhancement of yield stress and strain at break when comparing with the CIM sample, indicating a high strength and high toughness molded bars was obtained under the GAIM technique. This was probably due to the larger values of highly oriented zones and higher content of β-crystals in GAIM part.

Formation Mechanisms of hierarchical structures in GAIM

During the GAIM process, iPP crystallized from a melt that had been exposed to complex flow and temperature variations and the final specimen was characterized by an intrinsic heterogeneous microstructure, featuring a gradual and hierarchical variation of morphology that evolved throughout the part. The effect of shear field on the hierarchy structures of crystal is expected to depend on the extent of flow induced orientation and the rate at which this orientation relaxes ($\tau \cdot \gamma'$) [58]. According to the shear facilitates the formation of β-crystals [31-33] and the model of "Row nucleated structures" proposed by Janeschitz-Kriegl and co-workers [59], the morphological development of iPP under different shear strength was depicted in Fig. 13. As shown in Fig. 13a, under no shear or low shear ($\tau \cdot \gamma' \ll 1$), there were no shearing prenuclei and only some random point nuclei existed and finally α-spherulites were obtained. At medium shear ($\tau \cdot \gamma' < 1$), shear flow promoted local chain alignment and generated some precursors with an intermediate degree of order. These precursors composed of locally oriented, stretched chain segments and chains may be the "prenuclei" of amorphous character proposed by Varga and Karger-Kocsis [60], or the quasi-ordered clusters whose size and orientation distribution strongly depend on the intensity of the flow field [61], or the oriented, metastable and noncrystalline phase [62]. Point nuclei (under shear flow) came from shear prenuclei, which were aligned parallel to flow direction, and can facilitate the formation of β-spherulites as shown in Fig. 13b. At strong shear ($\tau \cdot \gamma' > 1$), when the applied shear stress exceeds the critical shear stress, threadlike nuclei formed. The high aspect ratio of the threads causes lamellar growth from them to be laterally constrained, resulting in formation of a highly oriented, row-nucleated morphology (β-cylindrites). At very high strong shear ($\tau \cdot \gamma' \gg 1$), a lot of threadlike nuclei were formed and the lamellar growth from them was highly laterally constrained and then shish-kebab can be obtained. Cylindritic structure and shish-kebab structure are developed via homogeneous or self nucleation and the main difference between them is that the density of row nuclei or threadlike nuclei.

To understand the different crystalline structure formation during the GAIM

process, the flow behaviors in the separated filling stages (such as, short shot and gas penetration process) should be made clear. The molecular chains were exposed to the shear field during both of the short shot and gas penetration process. And it is proved by our previous researches that the short shot process mainly affected the superstructures near the mold surface and gas penetration process played a dominating role on the crystalline structures away from the mold surface [13-15]. A schematic illustration of the shear rate profile in GAIM was shown in Fig. 14. As indicated in Fig. 14, the shear rate shown a sharp enhancement from the skin layer and reached its maximum at the sub-skin layer. Then, it began to fall to the minimum at the gas-channel layer. Based on these analysis and the morphological results, the diagram of hierarchical structures of GAIM part was depicted in Fig. 14. The shear strength was considered to be critical for the formation of β-spherulites, β-cylindrites and shish-kebab structure in the pure iPP specimen. When $\tau \cdot \gamma'$ was high enough, shish-kebab structures were formed. As the value of $\tau \cdot \gamma'$ decreased, β-cylindrites and β-spherulites appeared. When there was no shear or low shear, β-crystals disappeared and α-spherulites dominated in the corresponding area.

Conclusion

The orientation behavior, hierarchical distribution of β-crystals and mechanical properties of neat iPP molded by GAIM were intensively investigated in this research. A spatial variation of the superstructure with changed orientation and crystalline morphology along the thickness direction of molded bar was developed due to the interaction between the temperature field and shear field. It was for the first time found that the shish-kebab and β-cylindrite morphology coexisted at the sub-skin layer of GAIM part, where the shear strength was the greatest. More importantly, an neat iPP specimen with β-crystals existed in the whole cross section of the molded bars was obtained for GAIM sample, while for CIM sample, a low value of β-crystals was only found in the skin layer. In addition, when comparing with CIM sample, the yield stress of GAIM sample was greatly increased, accompanying with a sharp enhancement (five times) of the strain at break. These results firmly authenticated that

a high strength and high toughness sample was obtained for GAIM specimen due to a larger value of highly oriented zone and higher content of β-crystals. Finally, a schematic illustration was proposed to interpret the formation mechanism of the unusual hierarchical distribution of β-crystals in GAIM parts.

Acknowledgement

This work is financially supported by the National Natural Science Foundation of China (Grant No. 21174092, 20874066 and 51121001). We acknowledge the assistance of Mr. Chao-liang Zhang from the Huaxi College of Stomatology, Sichuan University for SEM experiments.

References

[1] A. Kelle, H. W. H. Kolnaar, In: Meijer HEH, editor. Processing of polymers, vol. 18. New York: VCH; 1997.

[2] R. H. Somania, L. Yang, L. Zhu, B. S. Hsiao, *Polymer*, 2005, **46**, 8587.

[3] X. F. Wei, R. Y. Bao, L. G, Y. Wang, K. Ke, W. Yang, B. H. Xie, M. B. Yang, T. Zhou, A. M. Zhang, *RSC. Adv.*, 2014, **4** , 2733.

[4] H. Fukushima, Y. Ogino, G. Matsuba, K. Nishida, T. Kanaya, *Polymer*, 2005, **46**, 1878.

[5] K. Zhang, Z. Y. Liu, B. Yang, W. Yang, Y. Lu, L. Wang, N. Sun, M. B. Yang, *Polymer*, 2011, **52**, 3871.

[6] L. Xu, Y. F. Huang, J. Z. Xu, X. Ji, Z. M. Li, *RSC. Adv.*, 2014, **4**, 1512.

[7] G. Kalay, M. J. Bevis, *J. Polym. Sci., Part B: Polym. Phys.*, 1997, **35**, 241.

[8] G. Kalay, P. Zhong, P. Allan, M. J. Bevis, *Polymer*, 1996, **37**, 2077.

[9] J. Avery, Gas-assist injection molding: principles and application. Munich: Hanser publishers; 2001

[10] G. Q. Zheng, L. Huang, W. Yang, B. Yang, M. B. Yang, C. T. Liu, C. Y. Shen, *Polymer*, 2007, **48**, 5486.

[11] L. Huang, W. Yang, B. Yang, M. B. Yang, H. N. An, *Polymer*, 2008, **49**, 4051.

[12] L. Wang, B. Yang, W. Yang, N. Sun, B. Yin, J. M. Feng, M. B. Yang, *Colloid. Polym. Sci.*, 2011, **289**, 1661.

[13] L. Wang, B. Yang, N. Sun, K. Zhang, J. M. Feng, M. B. Yang, *Colloid. Polym. Sci.*, 2012, **290**, 1133.

[14] G. Q. Zheng, W. Yang, L. Huang, Z. M. Li, M. B. Yang, B. Yin, Q. Li, C. T. Liu, C. Y. Shen, *J. Mater. Sci.*, 2007, **42**, 7275.

[15] G. Q. Zheng, W. Yang, C. T. Liu, C. Y. Shen, M. B. Yang, *Mater. Lett.*, 2007, **61**, 3436.

[16] C. Maier, T. Calafut, Polypropylene-the definitive user's guide and databook. Norwich: Plastics Design Library; 1998.

[17] B. Lotz, J. C. Wittmann, A. J. Lovinger, *Polymer*, 1996, **37**, 4979.

[18] A. J. Lovinger, J. O. Chua, C. C. Gryte, *J. Polym. Sci.:Polym. Phys. Ed.*, 1977, **15**, 641.

[19] K. Cho, D. N. Saheb, H. Yang, B. Kang, J. Kim, S. Lee, *Polymer*, 2003, **44**, 4053.

[20] H. B. Chen, J. Karger-Kocsis, J. S. Wu, J. Varga, *Polymer*, 2002, **43**, 6505.

[21] H. W Bai, Y. Wang, Z. J Zhang, L. Han, Y. L. Li, L. Liu, Z. W. Zhou, Y. F. Men, Macromolecules, 2009, 42, 6647.

[22] R. H. Somani, B. S. Hsiao, A. Nogales, S. Srinivas, A. H. Tsou, I. Sics, F. J. Balta-Calleja, T. A. Ezquerra, *Macromolecules*, 2000, **33**, 9385.

[23] R. H. Somani, B. S. Hsiao, A. Nogales, H. Fruitwala, S. Srinivas, A. H. Tsou, *Macromolecules*, 2001, **34**, 5902.

[24] P. W. Zhu, J. Tung, A. Phillips, G. Edward, *Macromolecules*, 2006, **39**, 1821.

[25] Q. X. Zhang, J. B. Song, S. Y. Wang, Z. S. Mo, *Polymer*, 2005, **46**, 11820.

[26] P. W. Zhu, G. Edward, *Macromol. Mater. Eng*., 2003, **288**, 301.

[27] H. W. Bai, Y. Wang, B. Song, Y. L. Li, L. Liu, *Polym. Eng. Sci.*, 2008, **48**, 1532.

[28] M. R. Kantz, H. D. Newman, F. H. Stigale, *J. Appl. Polym. Sci.,* 1972, **16**, 1249.

[29] D. R. Fitchmun, Z. Mencik, *J. Polym. Sci.:Polym. Phys. Ed.*, 1973, **11**, 951.

[30] H. Dragaun, H. Hubeny, H. Muschik, *J. Polym. Sci.:Polym. Phys. Ed.*, 1977, **15**, 1779.

[31] W. Wenig, F. Herzog, *J. Appl. Polym. Sci.*, 1993, **50**, 2163.

[32] Č. Roman, O. Martin, P. Petr, P. Martina, S. Karel, L. Anežka, *Eur. Polym. J.*, 2005, **41**, 1838.

[33] L. Wang, J. H. Wang, Y. Wang, B. Yang, Q. P. Zhang, M. B. Yang□, J. M. Feng, *Colloid. Polym. Sci*., 2013, **291**, 1503.

[34] B. Lee, T. J. Shin, S. W. Lee, J. Yoon, J. Kim, M. Ree, *Macromolecules*, 2004, **37**, 4174.

[35] B. Lee, T. J. Shin, S. W. Lee, J. Yoon, J. Kim, H. S. Youn, K. B. Lee, M. Ree, *Polymer*, 2003, **44**, 2509.

[36] R. H. Olley, D. C. Bassett, *Polymer*, 1982, **23**, 1707.

[37] J. X. Li, W. L. Cheung, D. Jia, *Polymer*, 1999, **40**, 1219.

[38] J. X. Li, W. L. Cheung, *Polymer*, 1998, **39**, 6935.

[39] A. Turner-Jones, J. M. Aizlewood, D. Beckett, *Makromol. Chem*., 1964, **75**, 134.

[40] R. H. Somani, L. Yang, B. S. Hsiao, T. Sun, N. V. Pogodina, A. Lustiger, *Macromolecules,* 2005, **38**, 1244.

[41] R. H. Somani, L. Yang, B. S. Hsiao, P. K. Agarwal, H. A. Fruitwala, A. H. Tsou, *Macromolecules*, 2002, **35**, 9096.

[42] K. Heo, J. Yoon, K. S. Jin, S. Jin, H. Sato, Y. Ozaki, M. M. Satkowski, I. Noda, M. Ree, *J. Phys. Chem. B*., 2008, **112**, 4571.

[43] Y. Y. Kim, K. Heo, K.-W. Kim, J. Kim, T. J. Shin, J. R. Kim, I. S. Yoon, M. Ree, *Macrmol. Res.*, 2014, **22**, 194.

[44] B. Ahn, T. Hirai, S. Jin, Y. Rho, K.-W. Kim, M.-A. Kakimoto, P. Gopalan, T. Hayakawa, M. Ree, *Macromolecules*, 2010, **43**, 10568.

[45] T. J. Shin, B. Lee, B. S. Seong, Y. S. Han, C.-H. Lee, H. H. Song, R. S. Stein, M. Ree, *Polymer*, 2010, **51**, 5799.

[46] H. D. Keith, F. J. Padden, J. N. M. Walter, H. W. Wyckoff , *J. Appl. Phys.*, 1959, **30**,1485.

[47] A. Kellar, J. Manchin, *J. Makromol. Sci. B1*, 1967, **B1**, 41.

[48] J. Varga, *J. Mater. Sci.*, 1992, **27**, 2557.

[49] A. J. Pennings, A. M. Kiel, *Kolloid-Z. Z. Polym.*, 1965, **205**, 160.

[50] F. Mai, K. Wang, M. J. Yao, H. Deng, F. Chen, Q. Fu, *J. Phys. Chem. B*., 2010, **114**, 10693.

[51] G. Shi, Z. Zhang, Y. Cao, J. Hong, *J. Makromol. Chem.*, 1993, **194**, 269.

[52] J. K. Keum, F. Zuo, B. S. Hsiao, *Macromolecules*, 2008, **41**, 4766.

[53] J. Varga, J. Karger-Kocsis, *J. Polym. Sci.: Part B. Polym. Phy*., 1995, 34, 657.

[54] J. Moitzi, P. Skalicky, *Polymer*, 1993, **34**, 3168.

[55] R. H. Somani, B. S. Hsiao, A. Nogales, H. Fruitwala, S. Srinivas, A. H. Tsou, *Macromolecules*, 2001, **34**, 5902.

[56] R. Su, J. X. Su, K. Wang, C. Y. Yang, Q. Zhang, Q. Fu Q, *Eur. Polym. J*. 2009, **45**, 747.

[57] J. Varga, *J. Macromol. Sci. Phys.*, 2002, **41**, 1121.

[58] A. Elmoumni, H. H. Winter, A. Waddon, H. Fruitwala, *Macromolecules*, 2003, **36**, 6453.

[59] S. Liedauer, G. Eder, H. Janeschitz-Krigel, *Int. Polym. Process.*, 1995, **3**, 243.

[60] J. Varga, J. Karger-Kocsis, *J. Polym. Sci: Part B. Polym. Phys.*, 1996, **34**, 657.

[61] B. J. Monasse, *J. Mater. Sci.*, 1992, **27**, 6047.

[62] R. Androsch, M. L. Di Lorenzo, C. Schick, B. Wunderlich, *Polymer*, 2010, **51**, 4639.

Figure Captions

Fig. 1 Schematic diagram of GAIM process: (a) partial melt filling; (b) gas-assisted filling; (c) gas-assisted packing.

Fig. 2 Schematic of sample preparation procedure for SAXS: FD, the flow direction; TD, the transverse direction; ND, the direction normal to the MD-TD plane.

Fig. 3 Shape and dimension of the GAIM molder bar.

Fig. 4 2D SAXS patterns at different zones of GAIM part: (a) the skin layer; (b) the sub-skin layer; (c) the gas channel layer, and CIM part, (d) the skin zone; (e) the core zone. The melt flow direction is parallel to the meridian direction.

Fig. 5 Azimuthal distribution of the scattered intensity in the 2D SAXS images of skin, sub-skin and gas channel layers of (G1, G2, G3) GAIM and skin and core layers of (C1, C2) CIM samples.

Fig. 6 1D SAXS intensity profiles of skin, sub-skin and gas channel layers of (G1, G2, G3) GAIM and skin and core layers of (C1, C2) CIM samples. Gx^{Eq} (x=1, 2) denotes the 1D SAXS intensity profiles along the equator, and Gx^{Mer} (x=1, 2) denotes the 1D SAXS intensity profiles along the meridian.

Fig. 7 PLM micrographs of the crystal morphologies in different zones of GAIM: (a) the whole picture; (b) near the skin zone; (c) near the gas channel zone; and CIM sample (d).

Fig. 8 SEM microphotographs of the crystalline morphologies of GAIM part: (a) skin layer; (b) sub-skin layer; (c) gas channel layer; (d) is the magnification of (b). The melt flow direction is parallel to the meridian direction.

Fig. 9 SEM microphotographs of CIM part: (a) skin layer; (b) core layer. The melt flow direction is parallel to the meridian direction.

Fig. 10 DSC heating curves of different zone of GAIM (a), and CIM parts (b).

Fig. 11 WAXD patterns of different layers of iPP molded by (a): GAIM; (b) CIM

Fig. 12 Strain-stress curves for GAIM and CIM parts.

Fig. 13 Schematic illustration of the morphological development of iPP under different shear strength.

Fig. 14 Schematic drawing of the shear rate profile during GAIM process and diagram of hierarchical structures of GAIM part. For brevity, the dimensionless distance was adopted and the number “0” and “1” denote the mold surface and gas channel, respectively.

Table Captions

Table 1 Processing variables used in the GAIM experiment.

Processing variables	Values
Gas pressure (MPa)	9.5
Gas delay time (s)	1.0
Gas packing time (s)	15
Short shot size (vol. %)	70
Melt temperature (°C)	210
Mold temperature (°C)	15
Injection pressure (MPa)	80

Table 2 Long spacing values at different zones of GAIM and CIM samples.

Samples	**GAIM**					**CIM**	
Zones	Skin		Sub-skin		Gas channel	Skin	Core
	L^{Eq}	L^{Mer}	L^{Eq}	L^{Mer}	L	L	L
long spacing (nm)	16.8	15.9	17.7	16.2	15.7	12.9	14.4

Table 3 The melting parameters of iPP at different layers.

	layer	ΔH_α J/g	X_α %	ΔH_β J/g	X_β %	ϕ_β %	K_β
GAIM	**skin**	66.01	37.29	8.15	4.84	11.48	0.28
	sub-skin	64.28	36.32	12.72	7.55	17.20	0.33
	gas channel	78.23	44.20	—	—	—	0.13
CIM	**skin**	69.97	39.53	—	—	—	0.06
	core	73.90	41.75	—	—	—	0

Table 4 Tensile properties for GAIM and CIM samples

Sample	Yield stress (MPa)	Yield strain (%)	Strain at break (%)
GAIM	43.0±2.1	16±2	460±45
CIM	32.2±1.4	12±2	95±12

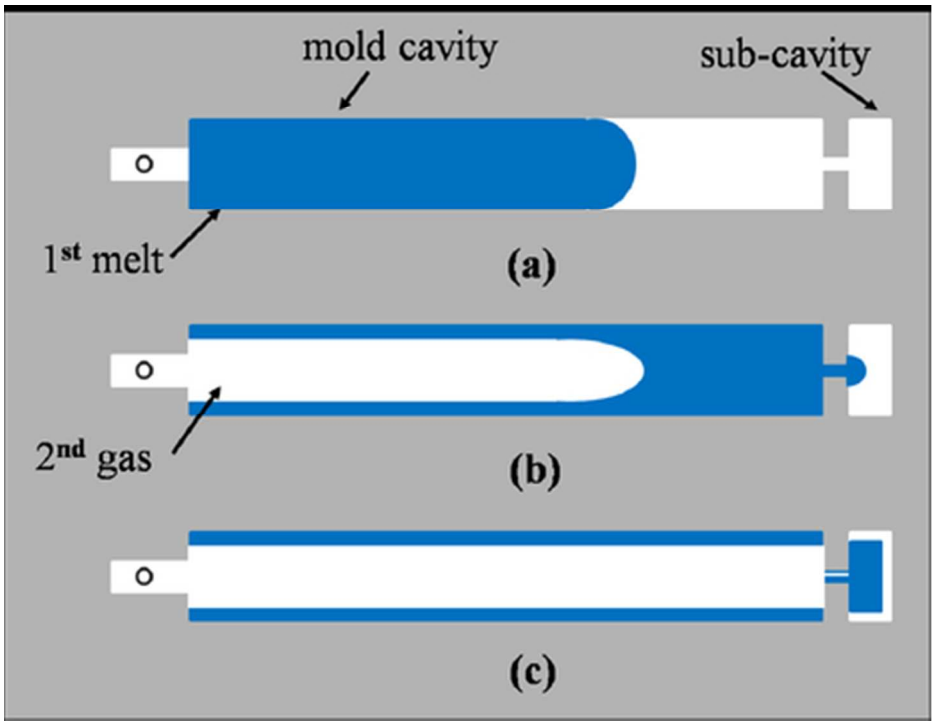

Figure 1
19x15mm (600 x 600 DPI)

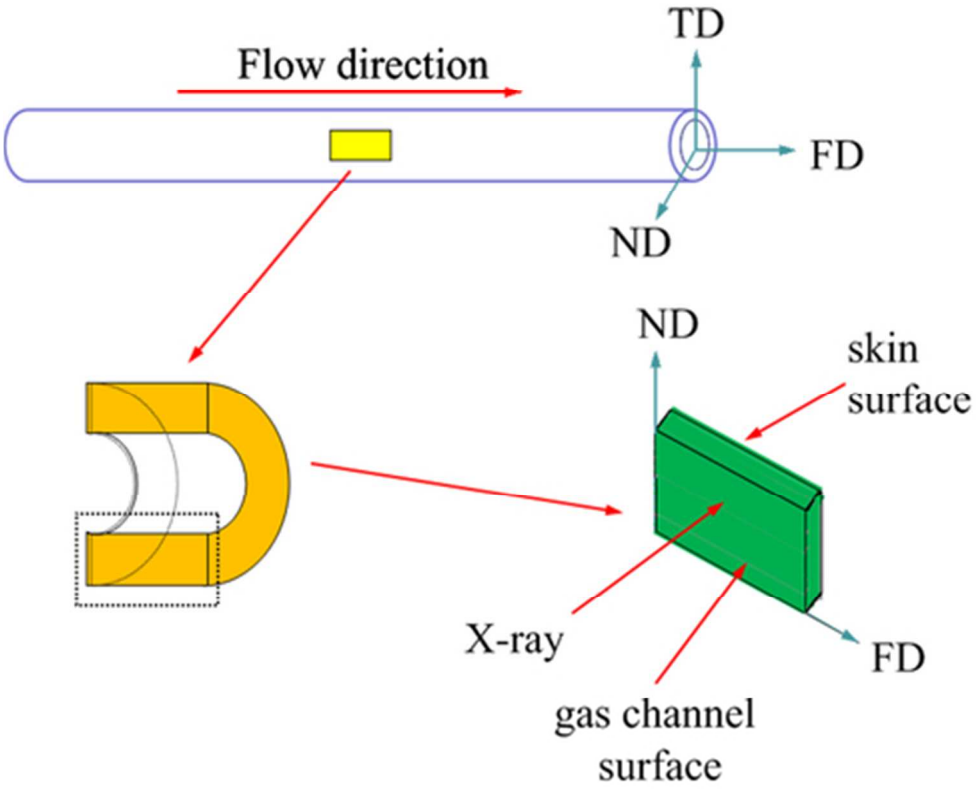

Figure 2
20x17mm (600 x 600 DPI)

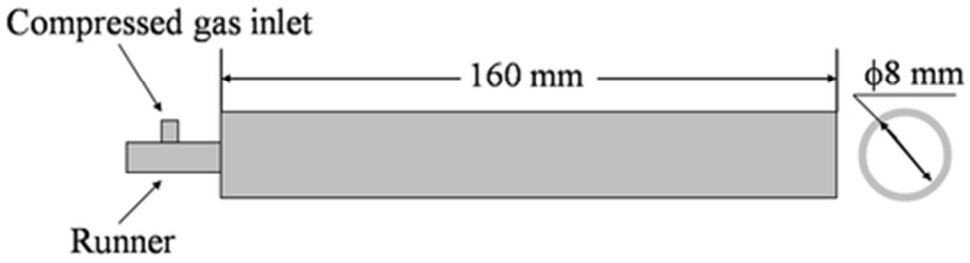

Figure 3
21x5mm (600 x 600 DPI)

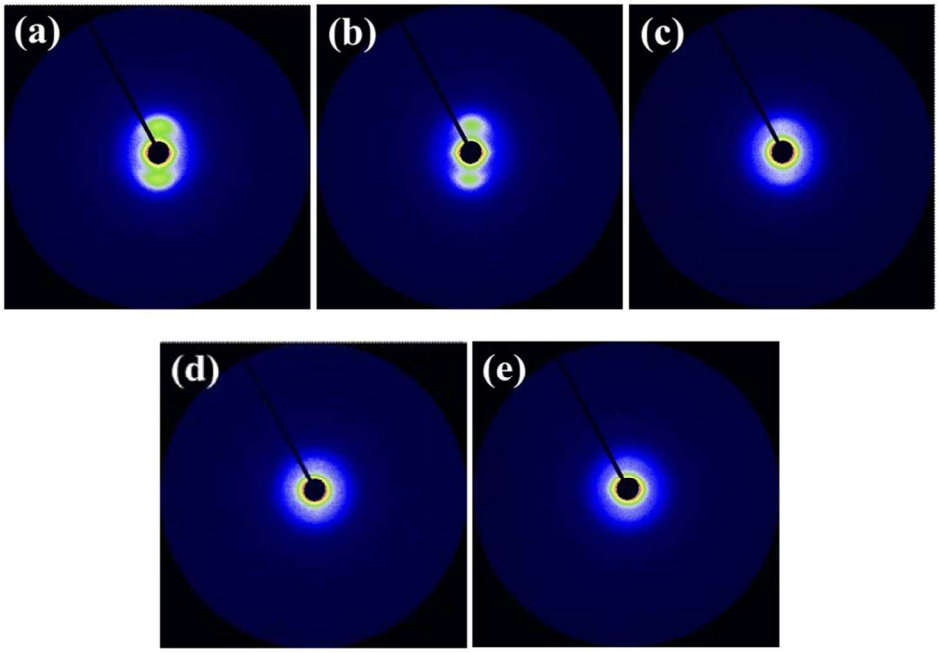

Figure 4
53x37mm (600 x 600 DPI)

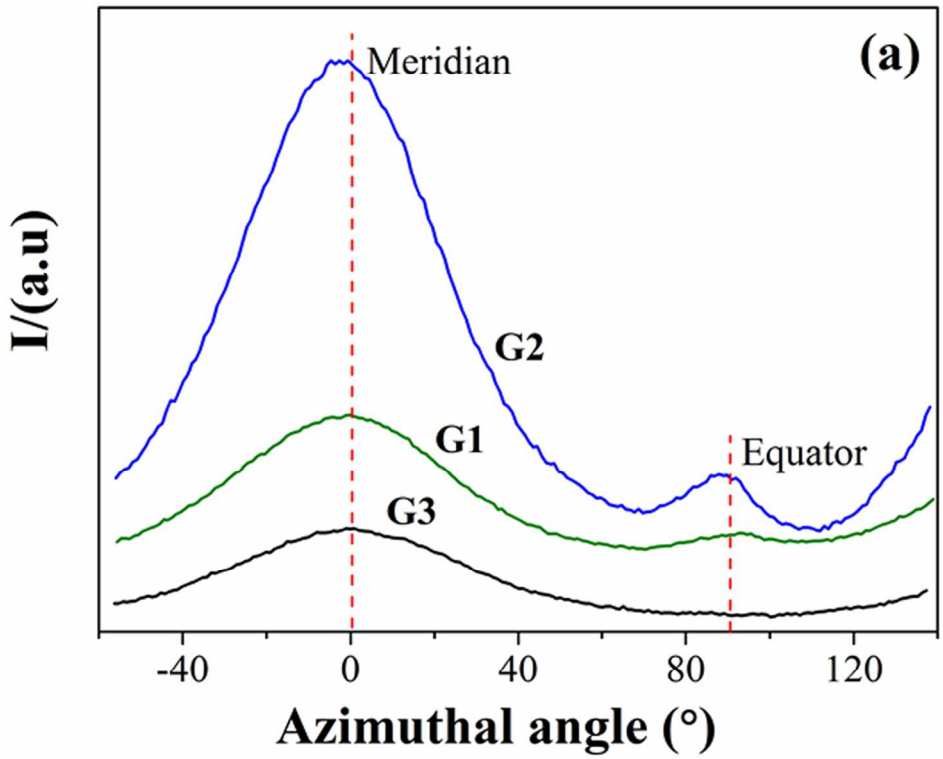

Figure 5(a)
60x47mm (600 x 600 DPI)

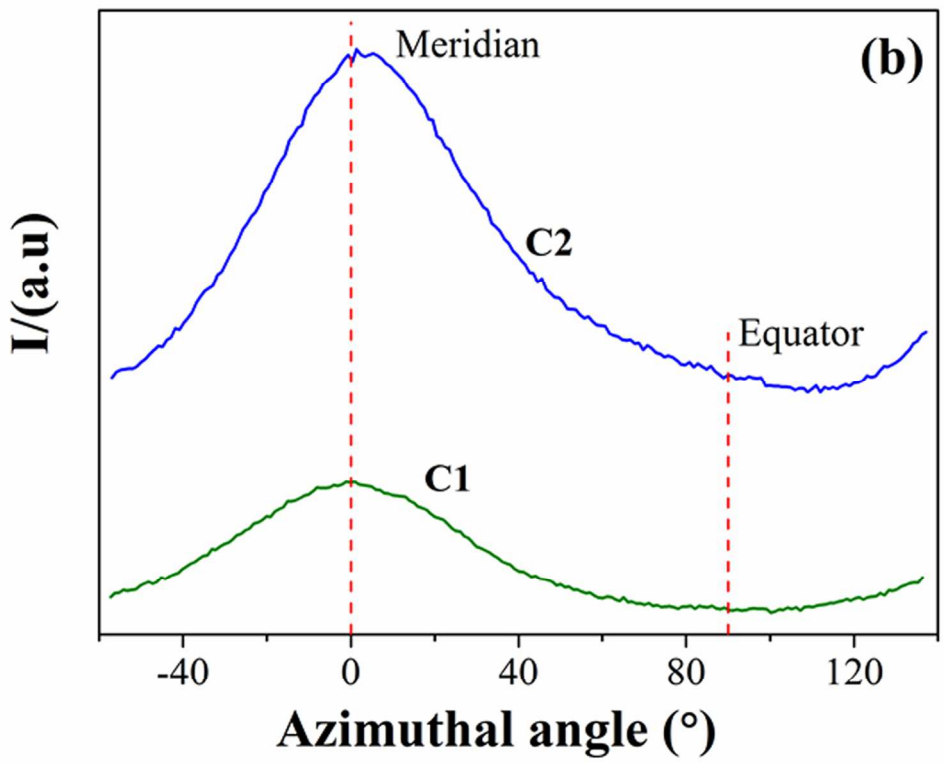

Figure 5(b)
60x47mm (600 x 600 DPI)

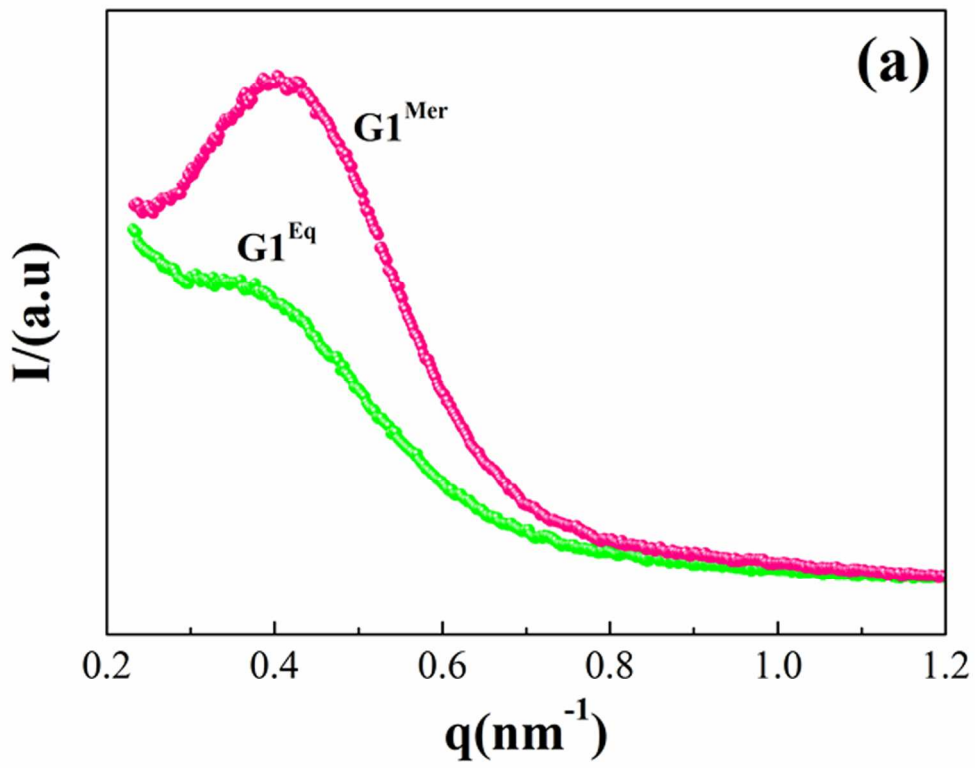

Figure 6(a)
60x47mm (600 x 600 DPI)

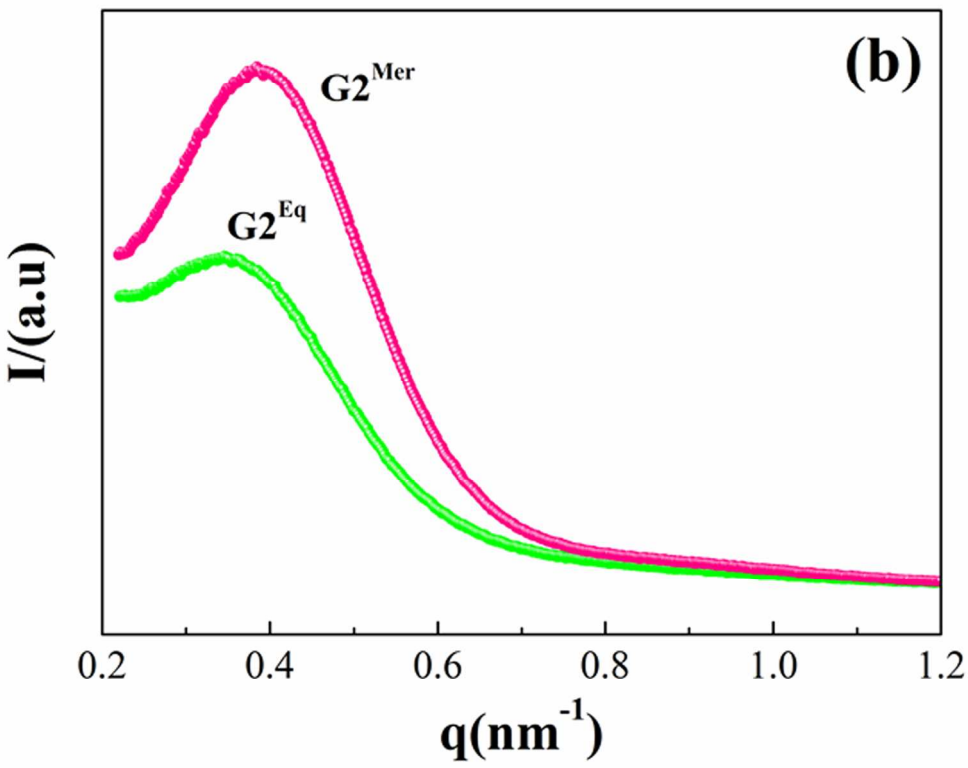

Figure 6(b)
60x47mm (600 x 600 DPI)

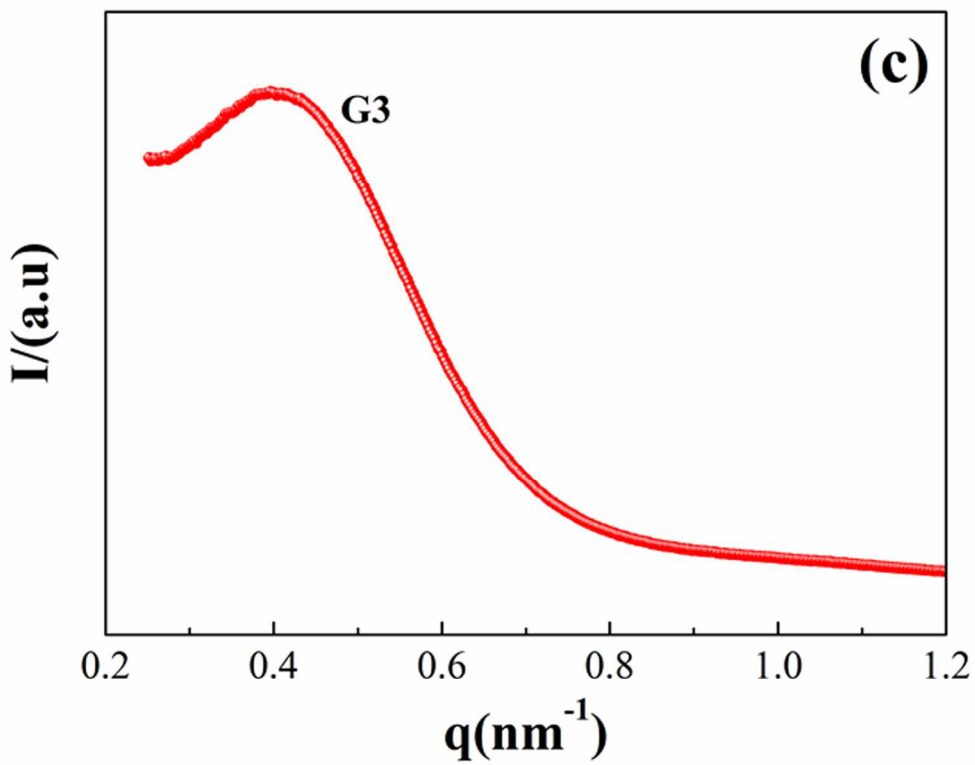

Figure 6(c)
60x48mm (600 x 600 DPI)

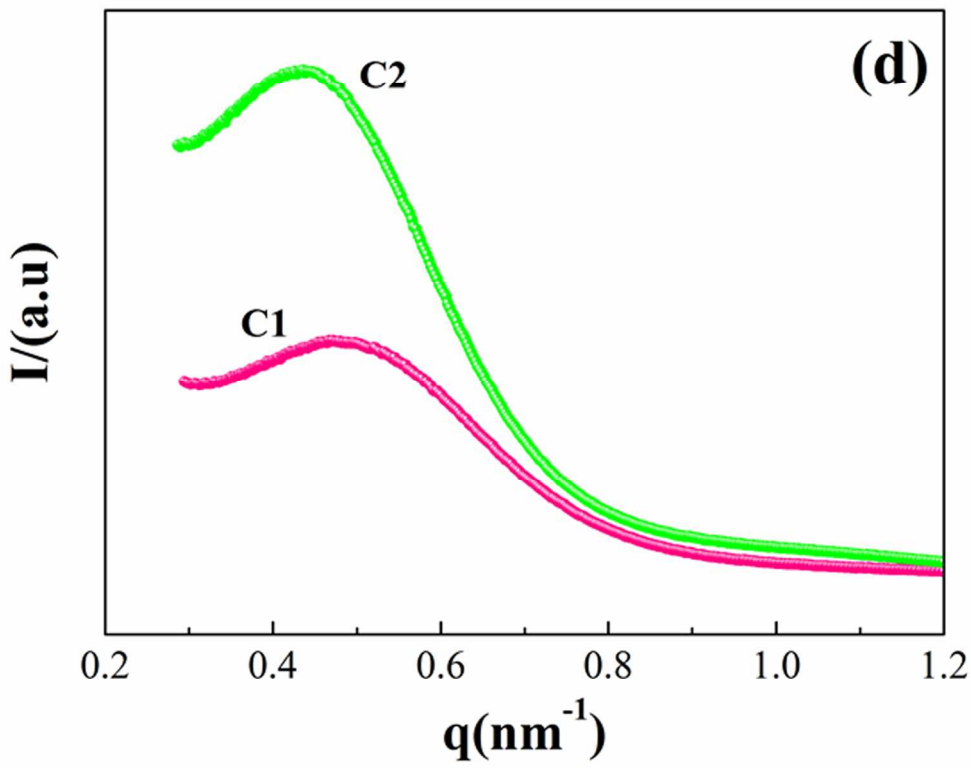

Figure 6(d)
60x47mm (600 x 600 DPI)

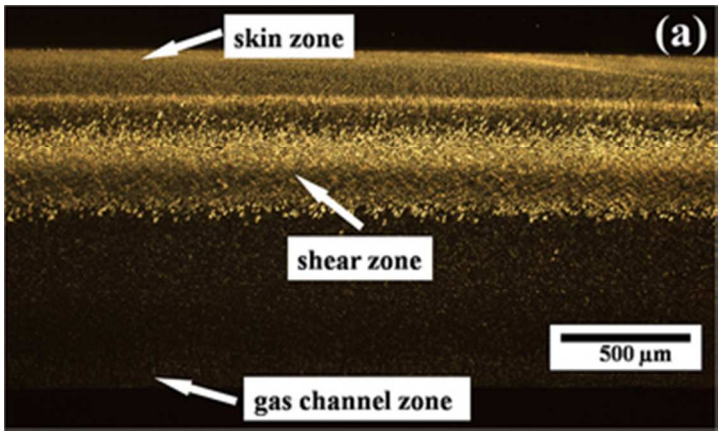

Figure 7(a)
15x8mm (600 x 600 DPI)

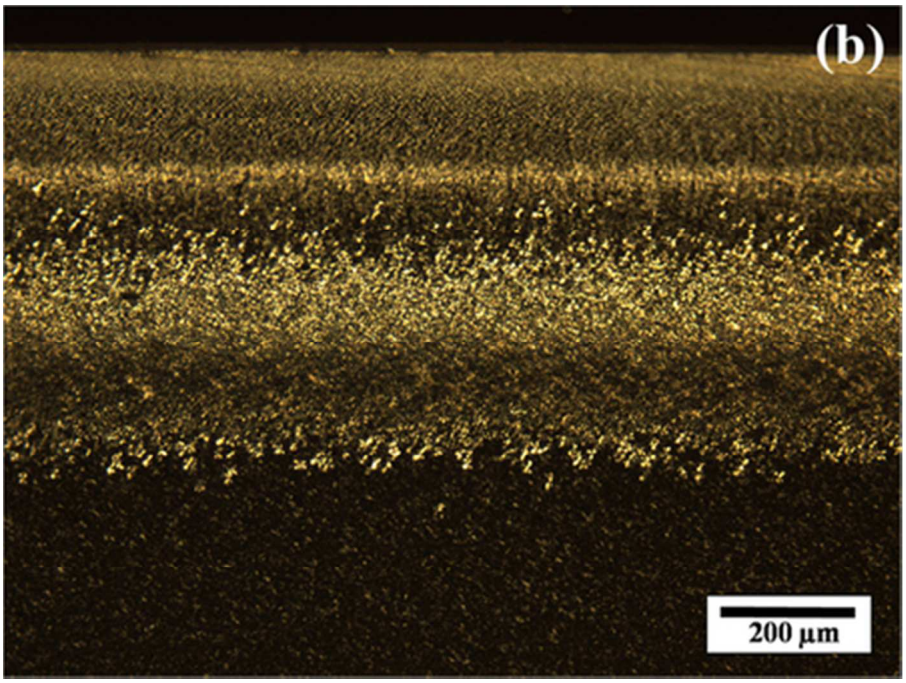

Figure 7(b)
19x14mm (600 x 600 DPI)

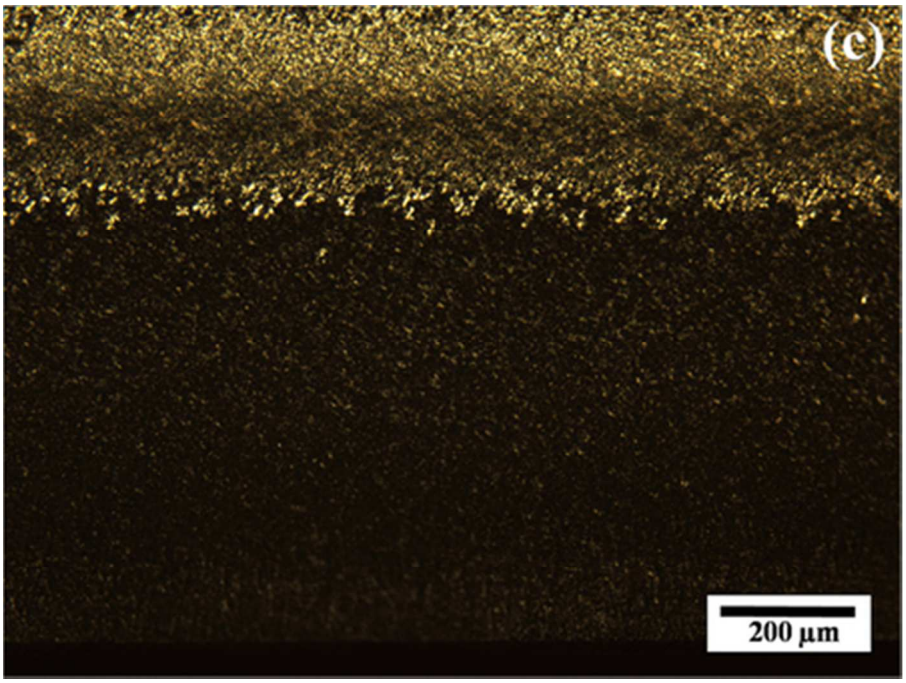

Figure 7(c)
19x14mm (600 x 600 DPI)

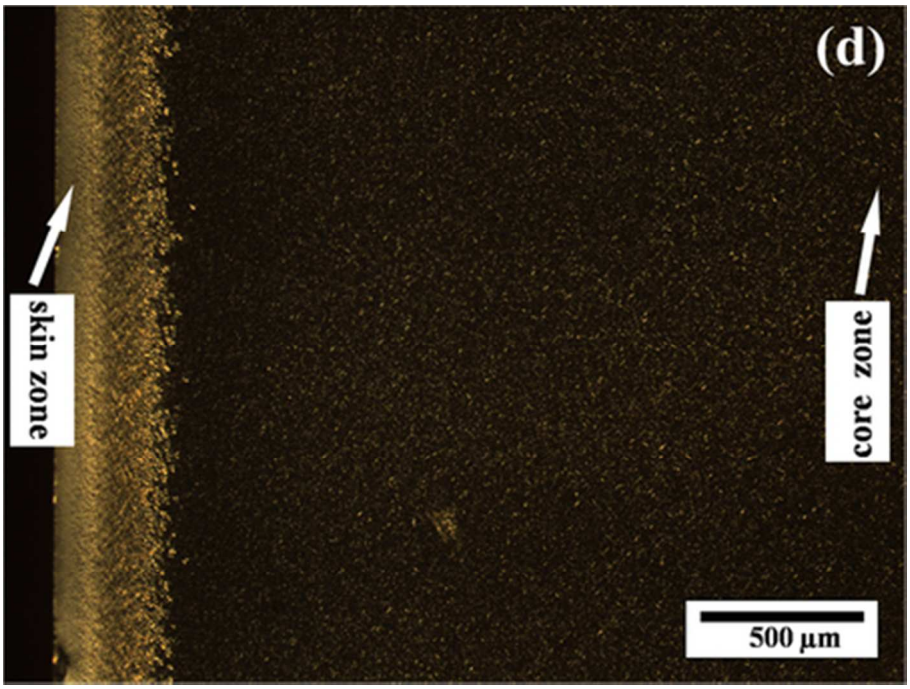

Figure 7(d)
19x14mm (600 x 600 DPI)

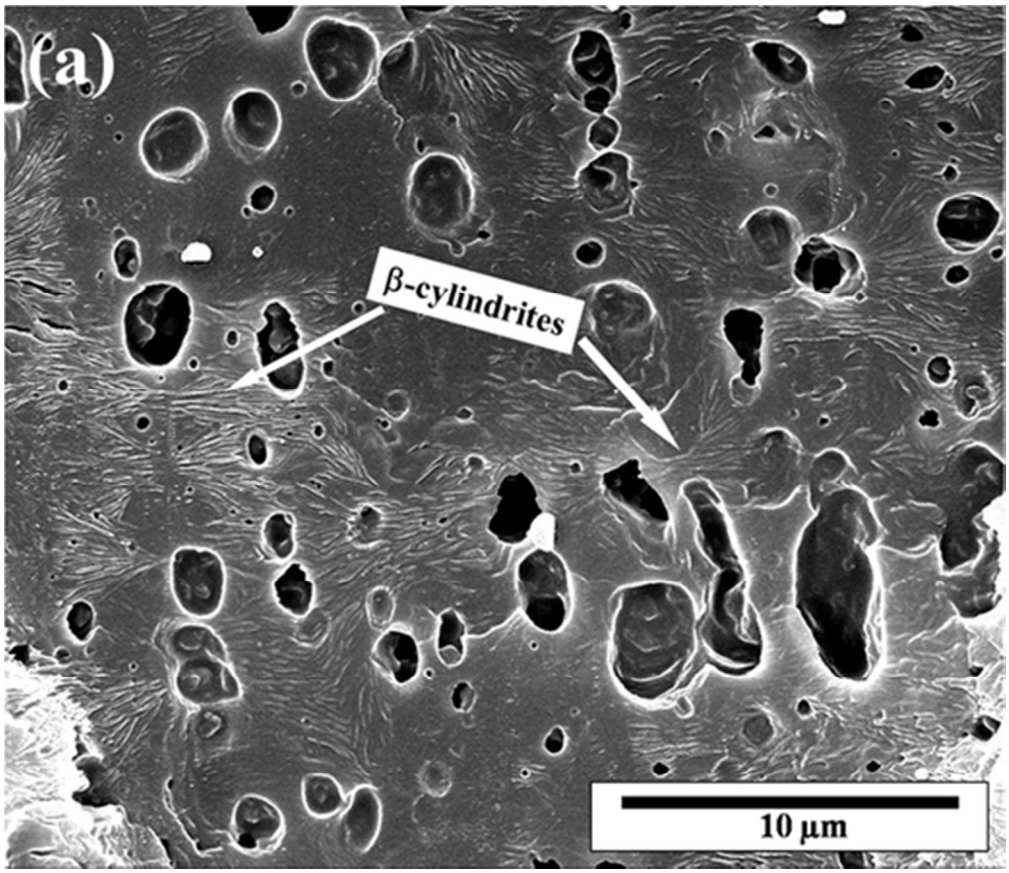

Figure 8(a)
21x18mm (600 x 600 DPI)

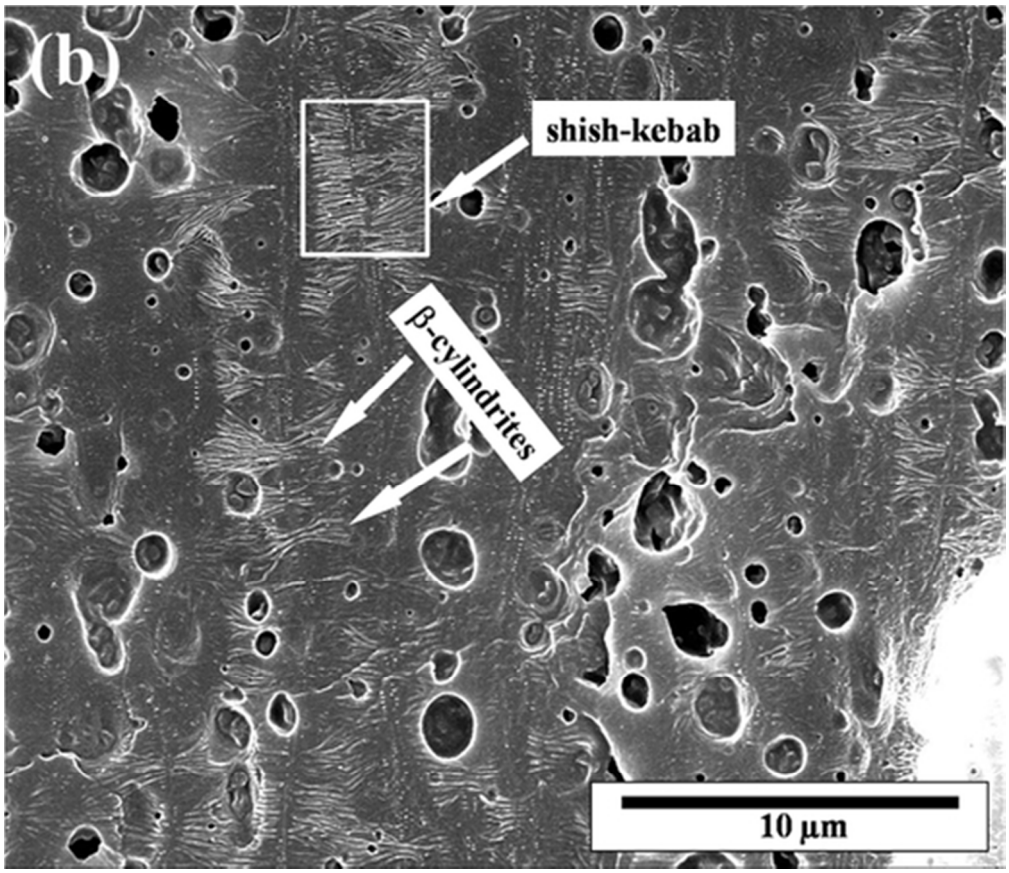

Figure 8(b)
21x18mm (600 x 600 DPI)

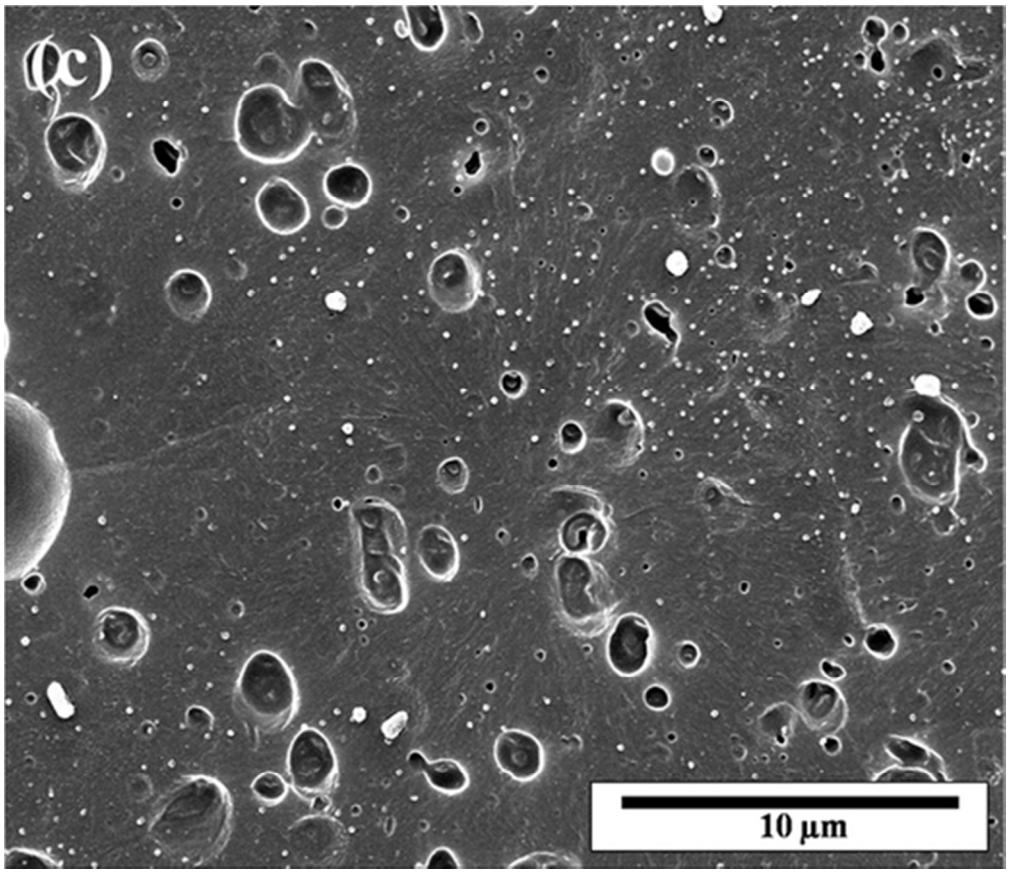

Figure 8(c)
21x18mm (600 x 600 DPI)

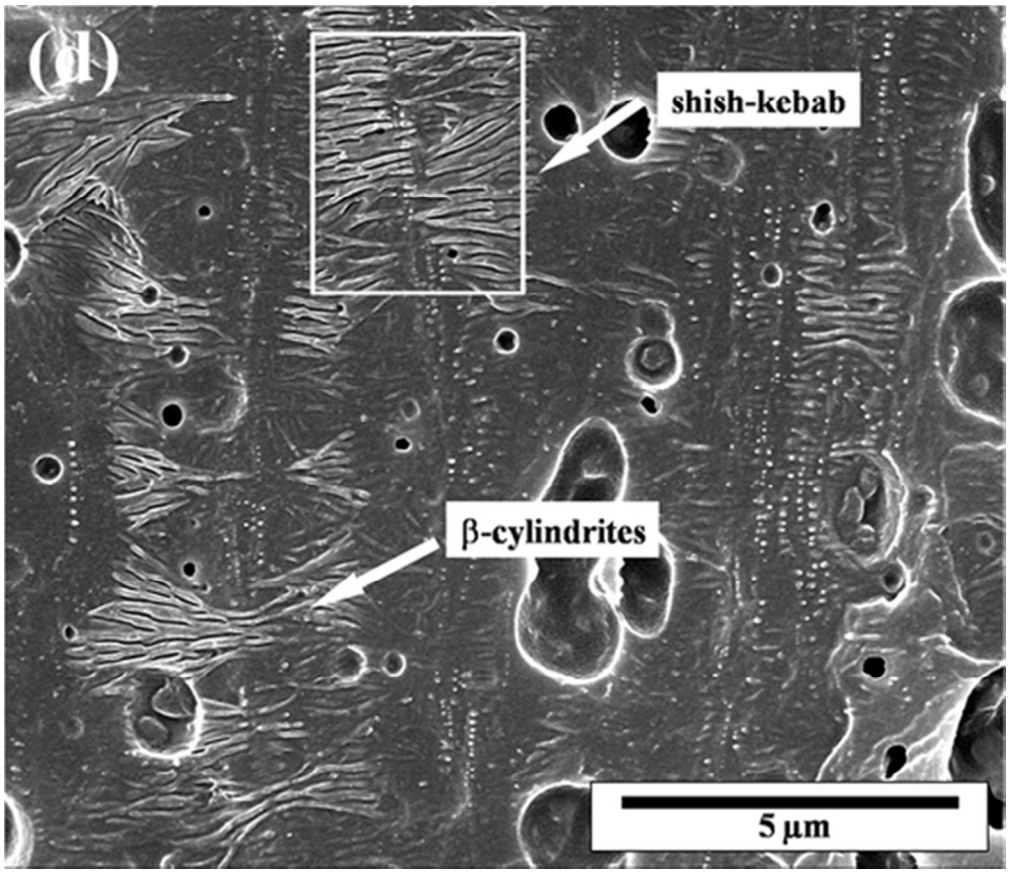

Figure 8(d)
21x18mm (600 x 600 DPI)

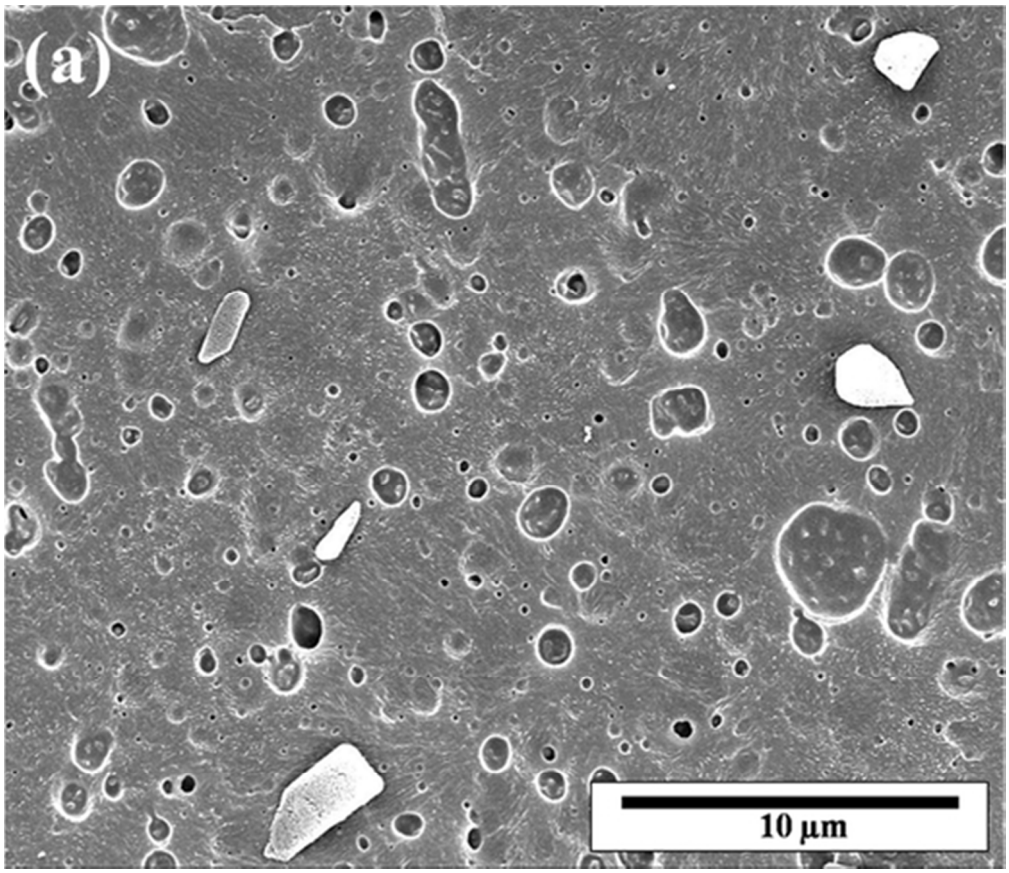

Figure 9(a)
21x18mm (600 x 600 DPI)

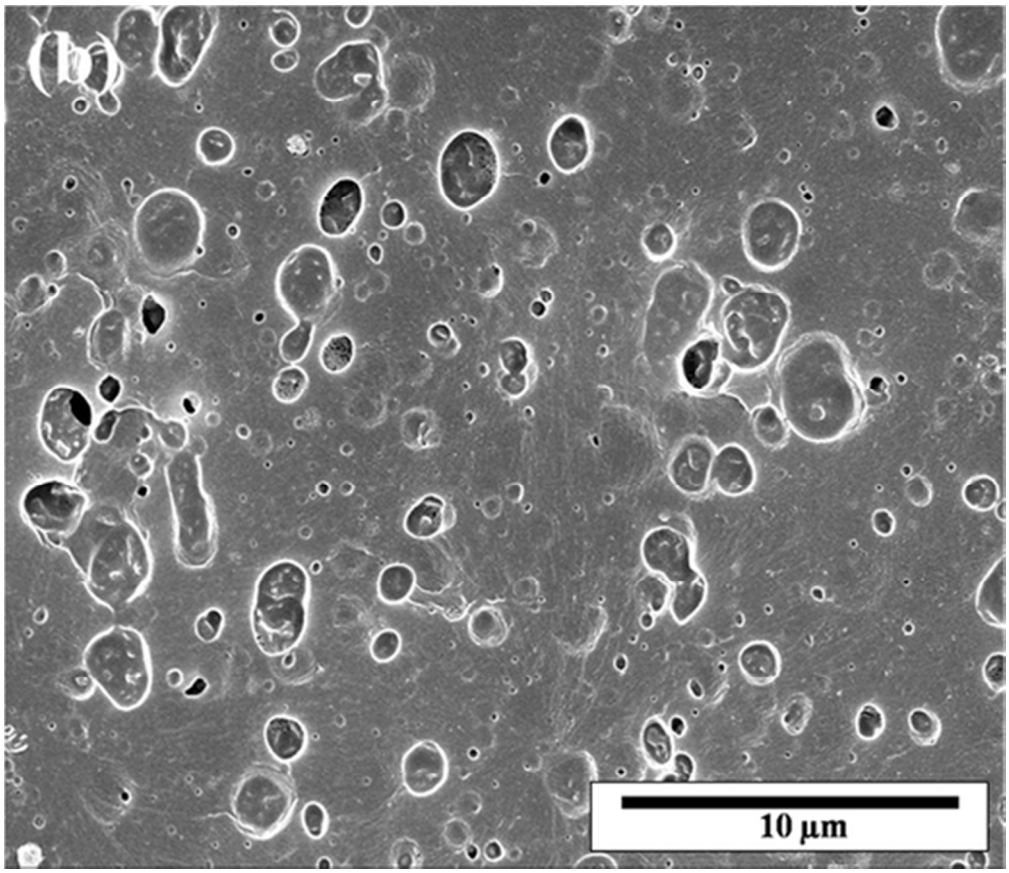

Figure 9(b)
21x18mm (600 x 600 DPI)

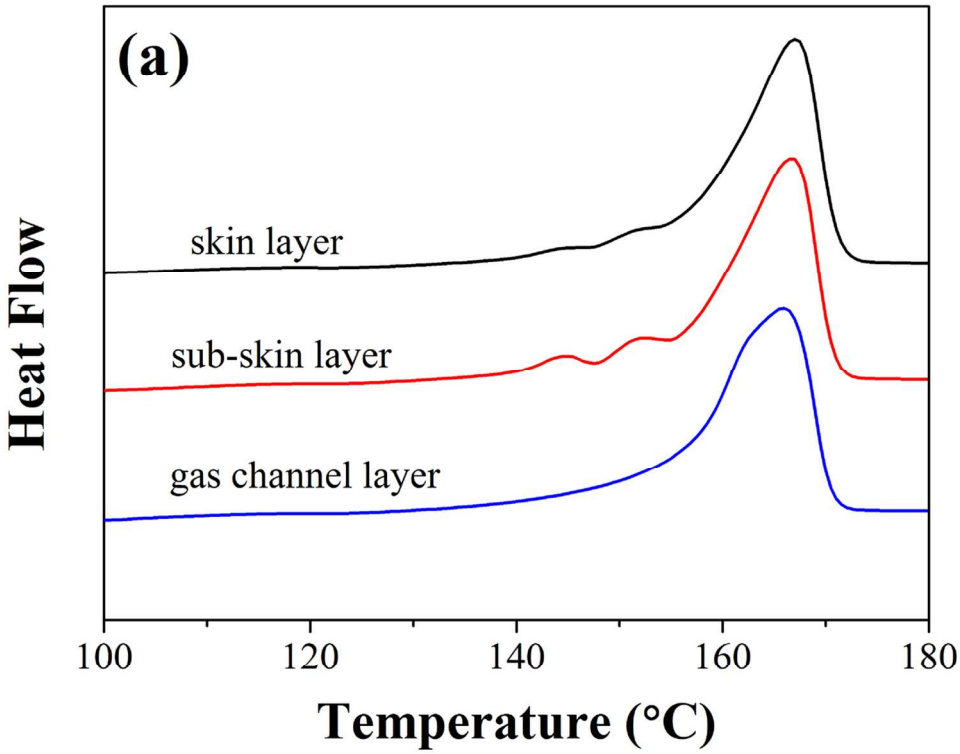

Figure 10(a)
119x93mm (300 x 300 DPI)

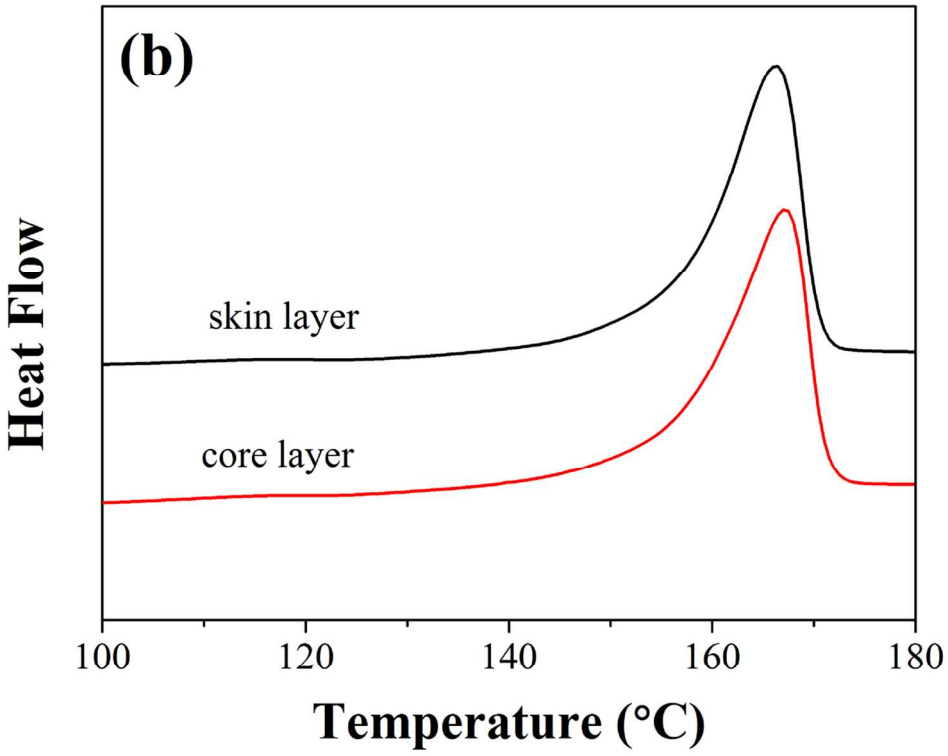

Figure 10(b)
119x93mm (300 x 300 DPI)

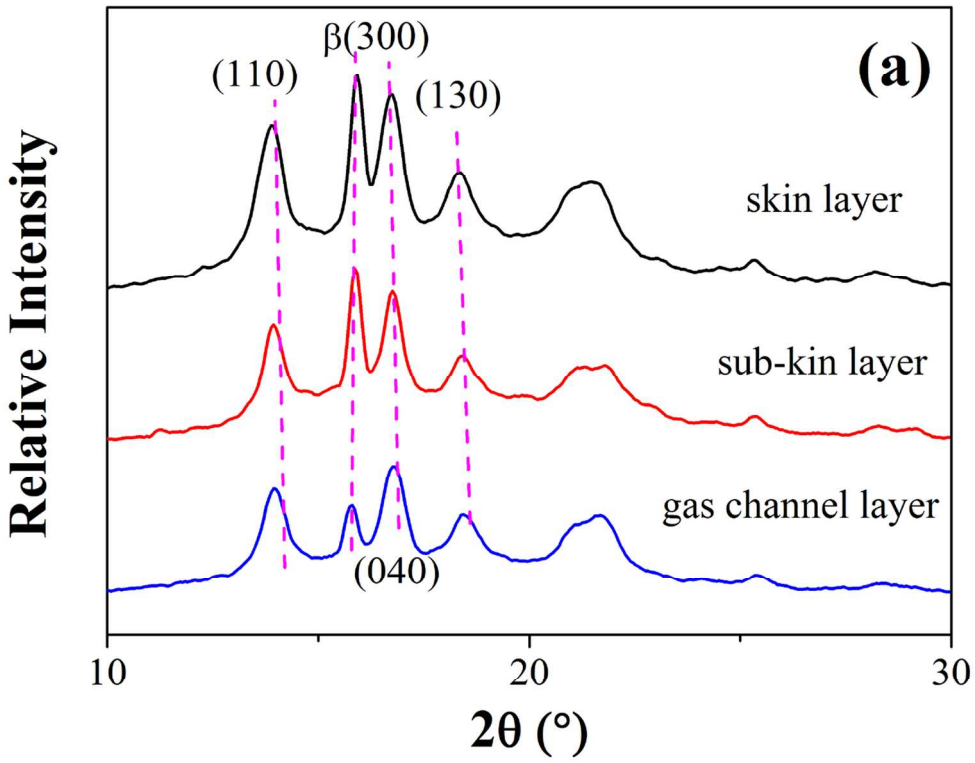

Figure 11(a)
122x98mm (300 x 300 DPI)

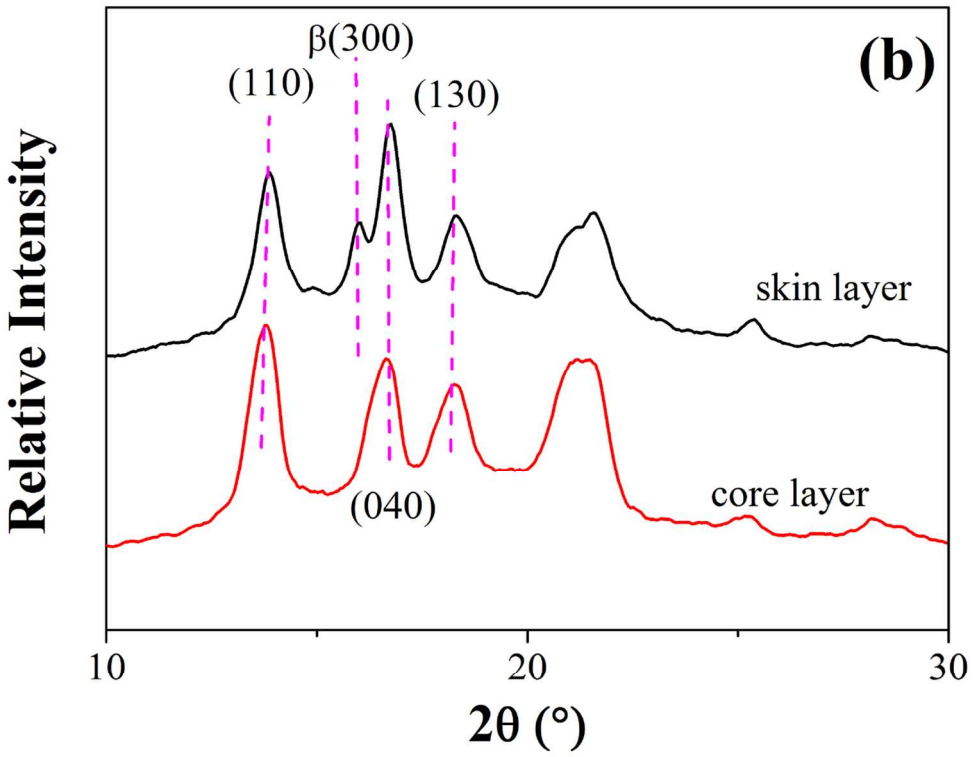

Figure 11(b)
122x98mm (300 x 300 DPI)

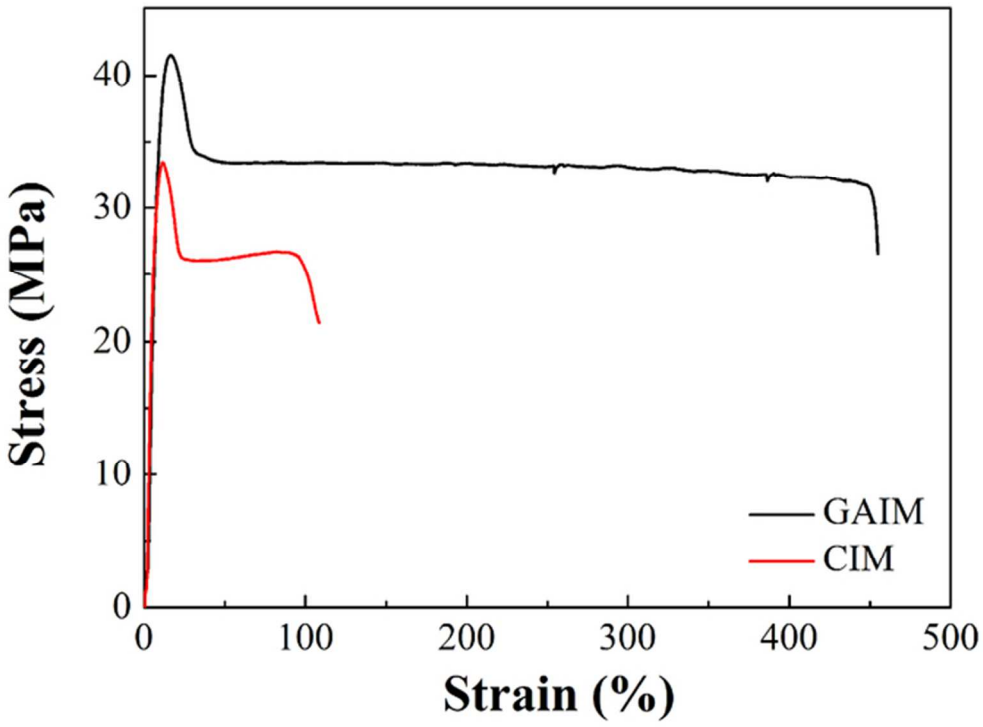

Figure 12
57x44mm (300 x 300 DPI)

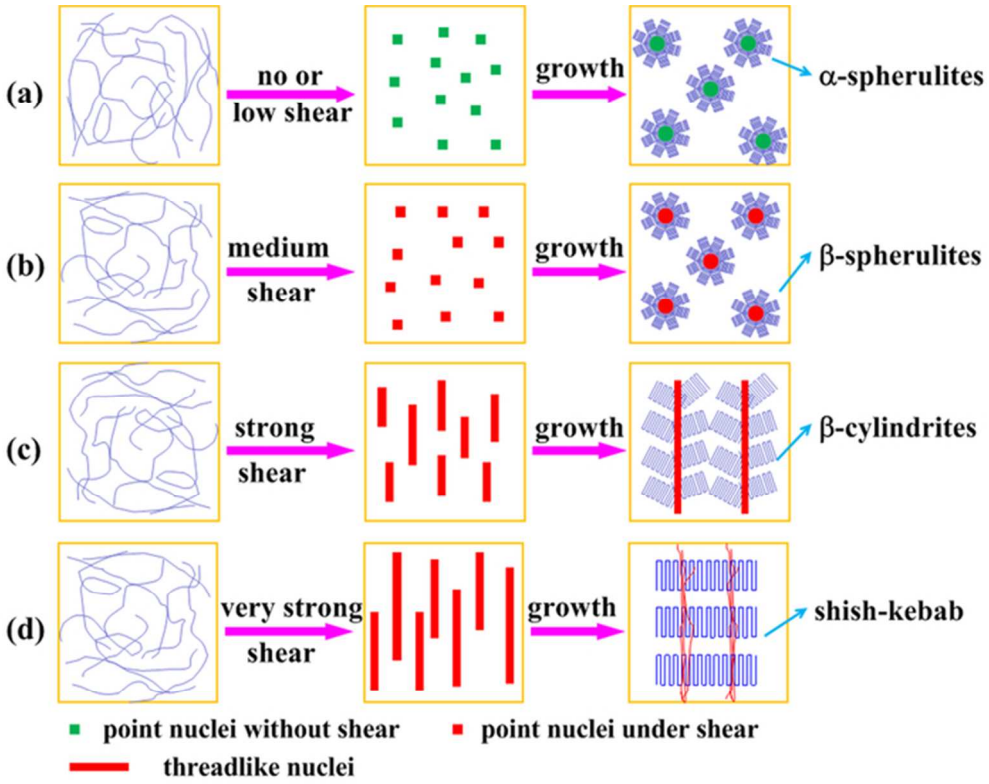

Figure 13
59x46mm (300 x 300 DPI)

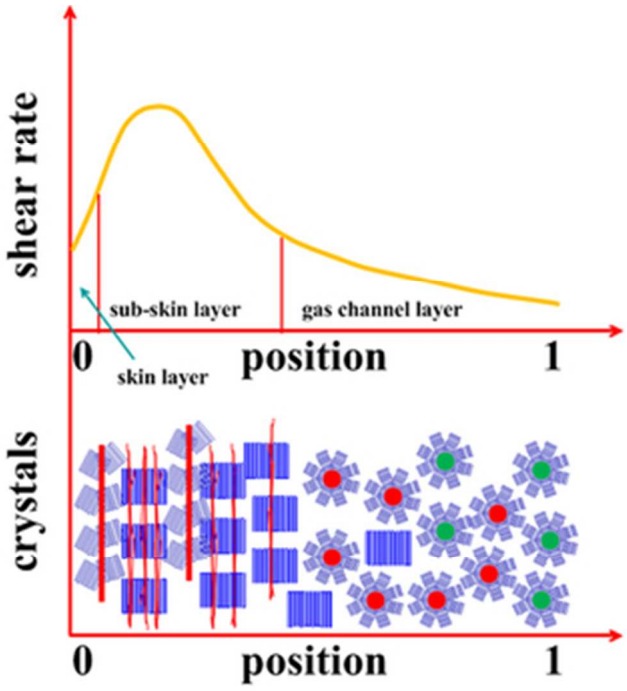

Figure 14
27x29mm (300 x 300 DPI)